Spring 5-13-2023

Analysis Of Ternary Chloride Salt Corrosion In High Nickel Alloys

Dimitri Madden
University of New Mexico

Gowtham Mohan
University of New Mexico

Dimitri Madden

Candidate

Mechanical Engineering

Department

This thesis is approved, and it is acceptable in quality and form for publication:

Approved by the Thesis Committee:

Gowtham Mohan, Chairperson

Kenneth Armijo, Committee Member

Pankaj Kumar, Committee Member

ANALYSIS OF TERNARY CHLORIDE SALT CORROSION IN HIGH NICKEL ALLOYS

BY

DIMITRI MADDEN

B.S. IN MECHANICAL ENGINEERING

THESIS

Submitted in Partial Fulfillment of the
Requirements for the Degree of

Master of Science in Mechanical Engineering

The University of New Mexico
Albuquerque, New Mexico

May, 2023

ACKNOWLEDGEMENTS

I would like to express my deepest gratitude to my committee members Dr. Gowtham Mohan, Dr. Kenneth Armijo, and Dr. Pankaj Kumar. Dr. Mohan, my advisor, has offered mentorship, assistance, and brought substantial experience to this work. Dr. Armijo has served as an unofficial advisor and offered me invaluable opportunities, guidance, and counsel, while also trusting me enough to take lead on this work. I thank Dr. Kumar for joining this committee and bringing his extensive skill set and expertise.

I owe great thanks to Dr. Youyang Zhao of the National Renewable Energy Laboratory and Dr. Patrick Burton of Sandia National Laboratories. Dr. Zhao, for his painstaking work consistently providing large quantities of purified salt for this project and Dr. Burton, for his significant support in post processing with handling, storing, cleaning, and assisting with the once unknown to me world of spectroscopy.

I would also like to thank partners at the University of Wisconsin Madison for their crucial assistance almost three years ago in the early stages of this work, helping develop the test system where their own designs and operating experience saved us from learning many hard lessons on our own.

Finally, I owe the greatest thanks to my partner in this work, Aaron Overacker, and to the rest of my peers at Sandia National Laboratories where this work was performed.

Sandia National Laboratories is a multi-mission laboratory managed and operated by National Technology & Engineering Solutions of Sandia, LLC, a wholly owned subsidiary of Honeywell International Inc., for the U.S. Department of Energy's National Nuclear Security Administration under contract DE-NA0003525.

ANALYSIS OF TERNARY CHLORIDE SALT CORROSION IN

HIGH NICKEL ALLOYS

by

Dimitri Madden

B.S., Mechanical Engineering, University of New Mexico, 2020

M.S., Mechanical Engineering, University of New Mexico, 2023

ABSTRACT

The United States Department of Energy seeks to improve the efficiency of concentrating solar power technologies by employing thermal energy storage with operating temperatures above 700°C. To meet these goals, the National Solar Thermal Test Facility at Sandia National Laboratories has considered the use of a ternary molten chloride salt for sensible heat storage systems. While favored for low cost, good heat transfer properties, and stability at high temperature, ternary chloride salt also exhibits high corrosive attack. Components of a chloride salt storage system would include piping, valves, tanks, pumps, receivers, and heat exchangers, which would be exposed to high temperatures and an extremely corrosive environment. In this paper we identify several potential alloy candidates for constructing such components of a chloride salt system and review existing studies on corrosion. Then, we introduce a comprehensive primary research study at Sandia National Laboratories to evaluate the salt compatibility of these alloy candidates. Ultimately, this paper focuses on the findings for five of the most promising alloys for chloride salt component manufacturing.

TABLE OF CONTENTS

TABLE OF FIGURES

TABLE OF TABLES

CHAPTER ONE: TERNARY CHLORIDE SALT CORROSION, A REVIEW

The following chapter is a review paper submitted for publication as a journal article titled "Materials for Ternary Molten Chloride Salt Thermal Transport Flow Systems". As of January 2023, the paper has been recommended for publication and is pending final review.

1.1 Introduction

Concentrating solar power (CSP) technologies have evolved significantly since the first steam-based systems emerged during the 1960's and 1970's [1]. Modern CSP heliostat field and power block systems are more efficient, facilitating advanced thermodynamic cycles with >600 °C high decomposition temperature heat transfer fluids (HTF). With HTF chemistry and material advancements, the scale of modern CSP facilities now ranges from 1 MW facilities, like the Dahan plant in China [2], to the 377 MW Ivanpah facility in the United States [3]. CSP has a unique advantage over other solar industries, as this technology has large thermal energy storage (TES) capabilities with extended periods of operation at 12 hours or more [4]. Stored HTFs can be used on demand for power cycles like steam Rankine or Brayton, providing consistent electricity. To increase efficiency and Levelized Cost of Electricity (LCOE), the U.S. Department of Energy (DOE) Solar Energy Technologies Office (SETO) has established goals for Generation 3 CSP facilities to operate with TES at temperatures exceeding 700 °C. Current commercial molten nitrate HTFs reach up to 600 °C, while next-generation HTFs can reach 1000 °C for storage [5],[6]. The development of a Gen 3 CSP system has been extensively researched at the National Solar Thermal Test Facility (NSTTF) of Sandia National Laboratories (SNL) [7]. This research has considered the use of ternary molten chloride salt (20% NaCl/40% $MgCl_2$/40% KCl by mol wt %) at 750 °C for CSP applications. Thermal transport components of a ternary

chloride salt liquid pathway would include piping, valves, tanks, and pumps, and would be subject to extremely corrosive environments. Development would require specific alloys and materials with high strength and corrosion resistance during various operational modes and temperatures. In this paper we provide a review of previous work analyzing thermal-physical properties of high-temperature materials and reliability challenges such as corrosion of alloys. We have found that it is difficult to construct a complete understanding of alloy corrosion in ternary chloride salt across high temperature ranges. While valuable data has been collected from previous tests, there is a need for consistent test methodology across a relevant temperature range to identify best suited materials for DOE Gen 3 CSP systems.

1.2 Thermal Energy Storage in CSP

1.2.1 Background

Molten salt TES systems allow for substantial increases in CSP plant productivity by increasing operating durations, providing potential storage durations of 16-18 hours [4],[8]. Molten salt TES systems can be found in a variety of different CSP technologies such as solar power towers (SPT). SPTs can utilize HTFs with high volumetric energy storage capacities as they allow for large temperature differences between cold legs and receivers [9]. Historically, most CSP plants with TES have employed nitrate-based molten salts for storage durations up to 6 hours [10],[11]. Almost exclusively the salt utilized is the binary mixture (60% $NaNO_3$/ 40% KNO_3) “solar salt” [12]. However, solar salt and other common HTFs only allow average annual CSP plant efficiencies of approximately 16% [13]. A primary limiting factor is the degradation temperature of the HTFs used. Most HTFs in CSP cannot operate above 550-600 °C, where increasing the

operating temperature of these systems would lead to greater efficiency [14]. Therefore, the U.S. DOE has called for an increase in operating temperatures up to 750 °C.

Benoit et al have described the requirements of a good next-generation HTF for utilization in CSP [13]. First, a good HTF would require a low melting point, reducing energy inputs needed for heaters in tanks and piping, and a high operating temperature to ensure thermal stability and efficient thermal cycling. Second, a good HTF candidate will require relatively high thermal conductivity and specific heat capacity for efficient thermal storage, as well as low viscosity to reduce dynamic head and required work by pumps. Low working pressure, because of low melting point and low vapor pressure, is also desirable for thermal transport systems such as piping wall thickness. For these reasons, a halide ternary chloride salt is considered here, which is believed to be an excellent candidate for next generation CSP systems.

1.2.2 Ternary Chloride Salt

Ternary Na-Mg-K chloride salt is a low-cost [14], high-decomposition temperature HTF researched for CSP applications at Sandia National Laboratory's NSTTF. The characteristics of the chloride salt are fundamentally based on the composition of a base carnallite ($KMgCl_3$) salt [15]. To stabilize the salt and increase the decomposition temperature, $MgCl_2$ salt is added. This addition can have challenging thermo-physical attributes, particularly related to MgO precipitation in the presence of humidity [16],[17]. However, elevated decomposition temperature from added $MgCl_2$ makes the salt a desirable candidate for enhanced efficiency CSP systems. With the addition of sodium chloride mixture to the salt (20% NaCl/40% $MgCl_2$/40% KCl by mol wt %), an excellent candidate for sensible heat storage applications is formed.

Ternary Na-Mg-K chloride salt has a high boiling point and one of the lowest vapor pressures of all chloride salts, making it better suited for high temperature systems than historical heat transfer fluids [5],[6],[5, 18]. The higher melting temperature of the chloride salt does unfortunately mean that support heaters are necessary to avoid freezing in pipes. Yet the high melting temperature and relatively low vapor pressure allow the salt to be stable at temperatures exceeding 750 ºC in an inert cover gas, without requiring excessive total system pressures [5]. Chloride salts also have adequately high specific heat capacity, though not as high as nitrate salts [5],[19]. Finally, one of the primary benefits of chloride salts is a far lower cost per kilogram than other high temperature HTF candidates. Prices for Na-Mg-K chloride salts in 2018 were 0.35 $/kg or lower, making chlorides simultaneously the least expensive and one of the highest temperature range options for an HTF [5]. However, a significant issue with the use of chloride salts is high corrosion, elevated in the presence of oxygen or water.

Chloride ions introduce pitting corrosion and crevice attack to metals in a high chlorine environment. Chloride ion corrosion has been extensively studied on ferrous metals. Typically, ferrous metals form a surface-level bilayer passive film, the inner layer composed of Fe_3O_4 and the outer layer a precipitate γ-Fe_2O_3 [20]. The compact bilayer film forms in the presence of oxygen and protects the metal from corrosion. Chloride ions are of such a small radius that they can pass through the passivating film [21]. At this point, the film can no longer be maintained [22]. The actual following corrosion mechanisms are not well known and will vary depending on the composition of the alloy. However, the corrosion is generally accepted to be correlated with the presence of MgOHCl molecules, which form in the presence of water [15]. Due to the high hygroscopic nature of the salt, even contact with a small amount of air can result in dissolved

MgOHCl impurities in the salt. It is also understood that certain alloying elements can have a significant impact on the corrosion rate. High iron content alloys such as stainless steels will degrade rapidly in molten chloride salt. Chromium content is also an important factor as studies have shown high chromium dissolution into chloride salts. This phenomenon is demonstrated in a 2005 study by Li et al [23], which found that in a NaCl-KCl salt melt at 670 °C, ferrous metals containing high chromium content were detrimentally affected by the chromium and had high corrosion rates. This result was confirmed in a 2012 study by Vuelvas-Rayo et al, exposing high chromium content ferrous metals to NaCl-KCl at 670 °C and comparing the results to SS 304 [24]. The ferrous metals in the study had higher corrosion than SS 304, and degradation increased with increasing chromium content. Finally, an important factor to consider is the purity of the salt itself. The presence of air or water in or around the salt will result in impure salt containing MgOHCl, the primary corrosion mechanism. As demonstrated by Zhao [15], salt purity can be increased by dosing with magnesium at high temperature. This purified salt has been shown to have reduced corrosion on alloys [15].

1.3 Alloys for use in CSP Molten Salt Systems

Wetted components in a next generation chloride salt system must maintain adequate corrosion resistance for temperatures at or above 750 ºC. Halide chloride salts are highly corrosive at increasing temperature. This places an emphasis on proper material selection for highest temperature system components, such as CSP receivers which absorb the concentrated solar flux. Historically, CSP TES systems have been constructed of SS 316 and 304 [25], [26]. This is due to the excellent compatibility of nitrate solar salt with austenitic stainless steels in terms of strength and corrosion resistance at temperatures of 250 °C to 550 °C [27], [28]. Some

nitrate salt receivers have been designed for construction with Inconel, such as the Inconel 625 tubular receiver patented by Boeing in 1999 [26]. However, austenitic stainless steels were more common in engineering of heat exchangers and thin-walled nitrate salt flow components [29]. Many CSP TES systems were constructed utilizing a combination of stainless steels and solar salt, such as the Solar Two Pilot Plant [30]. Yet while stainless steel is effective for use with solar salt, it cannot reliably be used with ternary molten chloride salt or at temperatures exceeding 750 °C.

High nickel content within alloys, on the other hand, shows promise for chloride corrosion resistance. Nickel alloys are generally resistant to stress corrosion cracking and pitting corrosion in high chlorine environments [31]. The 2005 study by Li et al found that, of alloys tested, a NiAl sample had the best corrosion resistance with pure Ni also performing well [23]. Nickel alloys are also capable of incorporating a high amount of beneficial alloying elements for increased corrosion resistance [31]. A 1985 study by Oryshich and Kostyrko further investigated nickel alloy corrosion in chloride salts with the inclusion of refractory metals molybdenum, tungsten, and cobalt in the alloy composition [32]. The study found that alloys combining high nickel content with molybdenum, tungsten, and cobalt had better resistance to chloride corrosion. This study also noted the effect of chromium on corrosion, as alloys lacking refractory metals had high chromium dissolution in the salt, while the addition of the refractory metals resulted in 10 times less chromium dissolution. For these reasons, high nickel alloys are often considered as the primary candidates for use with halide chloride salts.

For this review, 12 alloy candidates were evaluated: Haynes 230, Inconel 617, Hastelloy C276, Inconel 625, Inconel 740H, Inconel 800H, Inconel 600, Hastelloy N, Haynes 282, SS 316,

SS 347H, and SS 304H. These alloys were selected for composition, relevance to CSP, and abundance of data. Table 1 shows the elemental composition of each considered alloy.

Table 1: Alloy Composition

	Haynes 230 [33]	Inconel 617 [34]	Hastelloy C276 [35]	Inconel 625 [36]	Inconel 740H [37]	Inconel 800H [38]	Inconel 600 [39]	Hastelloy N [40]	Haynes 282 [41]	SS 316 [42]	SS 347 [43]	SS 304 [44]
Nickel	57.00	44.50 Min	50.99-58.99	58.00 Min	37.85-52.73	30.00-35.00	72.00 Min	71.00	57.00	10.00-14.00	8.00-10.50	8.00-10.50
Chromium	22.000	20.00-24.00	15.00-16.50	20.00-23.00	23.50-25.50	19.00-23.00	14.00-17.00	7.00	20.00	16.00-18.00	17.00-20.00	18.00-20.00
Tungsten	14.00		3.00-4.50					0.50 Max				
Molybdenum	2.00	8.00-10.00	15.00-17.00	8.000-10.000	2.00			16.00	8.50	2.00-3.00		
Iron	3.00 Max	3.00 Max	4.00-7.00	5.000 Max	3.00	39.50	6.00-10.00	4.00 Max	1.50 Max	62.15-69.15	66.58-72.14	66.58-71.14
Cobalt	5.00 Max	10.00-15.00	2.50	1.00	15.00-22.00			0.20 Max	10.00			
Copper		0.50 Max			0.50		0.50	0.35 Max				
Manganese	0.50	1.00 Max	1.00	0.50	1.00		1.00	0.80 Max	0.30 Max	2.00	2.00	2.00
Silicon	0.40	1.00 Max	0.08	0.50	1.00		0.50	1.00 Max	0.15 Max	0.75	0.75	0.75
Aluminum	0.30	0.80-1.50		0.40	0.20-2.00	0.15-0.60		0.50 Max	1.50 Max			
Titanium	0.10 Max	0.60 Max		0.40	0.50-2.50	0.15-0.60		0.50 Max	2.10 Max			
Carbon	0.10	.05- .15	0.02	0.10	0.01-0.08	0.10 Max	0.10	0.06 Max	0.06 Max	0.03	0.04-0.10	0.04-0.10
Sulfur		0.02 Max	0.03	0.02	0.03		0.02			0.03	0.03	0.03
Phosphorus			0.03	0.02	0.03					0.05	0.05	0.05
Other	0.54 Max	0.01 Max	0.35	3.15-4.15	0.60-2.60			0.50	0.01	0.10		0.10

All alloys considered have significant chromium composition. However, several of the alloys presented also have nickel content near or above 50%. Some of these alloys have high

tungsten, molybdenum, and cobalt content. As discussed, these elements play a key role in corrosion resistance to chlorides.

1.3.1 Alloy Corrosion

Chloride corrosion is accelerated with both increasing temperature and varying atmospheric conditions. For this reason, the proper combination of salt, alloy, and either inert cover gas or vacuum environment is crucial to corrosion mitigation for high temperature applications. An extensive literature review was conducted at the NSTTF in search of published chloride salt corrosion data for the previously listed alloys. Useful data was compiled for varying salt chemistries, test setups, atmospheric conditions, temperatures, and exposure durations. This data is summarized in Table 2. Note this table was strictly compiled with data for alloys of interest, in $MgCl_2$, NaCl, or KCl, and reported in µm or mass loss corrosion units.

Table 2: Alloy Corrosion

Alloy	Cover Gas	Salt	Temp. (°C)	Duration (hours)	Corrosion (mg/cm^2)	Corrosion (µm/year)	Corrosion/ Chromium Depletion Depth (µm)	Source
Ni200	Air	$MgCl_2$-NaCl	520	140		57		[45],[46]
Haynes 230	Argon	$MgCl_2$	750	100		114.92	18	[47]
	Argon	$MgCl_2$	750	200		53.03	14	[47]
	Argon	$MgCl_2$	750	500		24.28	14	[47]
	Argon	$MgCl_2$	750	1000		7.98	19	[47]
	Argon	KCl-$MgCl_2$	800	384		16.14		[48]
	Argon	KCl-$MgCl_2$-NaCl	600	400	0.55		25	[49]
	Argon	KCl-$MgCl_2$-NaCl	700	400	2.7		100	[49]
	Argon	KCl-$MgCl_2$-NaCl	800	400	-0.26			[49]
	Nitrogen	KCl-$MgCl_2$-NaCl	800	100		27	31.6	[15]
	Nitrogen	KCl-$MgCl_2$-NaCl + 0.1 wt.% Mg	800	100			7.97	[15]
	Vacuum	$MgCl_2$-KCl	850	100	6.9			[50]
Inconel 625	Argon	$MgCl_2$	750	100		155.13	18	[47]
	Argon	$MgCl_2$	750	200		66.80	21	[47]

	Argon	$MgCl_2$	750	500		33.71	26	[47]
	Argon	$MgCl_2$	750	1000		8.55	42	[47]
Hastelloy C276	Argon	KCl-$MgCl_2$-NaCl	700	500		79	30	[51]
	Argon	KCl-$MgCl_2$	800	384		10.03		[48]
	Argon	KCl-$MgCl_2$-NaCl	600	400	0.39			[49]
	Argon	KCl-$MgCl_2$-NaCl	700	400	1.49		25	[49]
	Argon	KCl-$MgCl_2$-NaCl	800	400	1.48		50	[49]
Inconel 800H	Argon	KCl-$MgCl_2$-NaCl	700	500		364	50	[51]
	Vacuum	KCl-$MgCl_2$	850	100	13.1			[50]
Inconel 600	Argon	NaCl-KCl	700	300			330	[52]
	Vacuum	KCl-MgCl2-NaCl	500	1000	0.27			[53]
	Vacuum	KCl-MgCl2-NaCl	500	1000	0.45			[53]
	Vacuum	KCl-$MgCl_2$	850	100	14.8			[50]
SS 316	Argon	NaCl-KCl	500	240	0.37	17.12		[54]
	Argon	NaCl-KCl	600	240	0.8	38.28		[54]
	Argon	NaCl-KCl	700	240	4.49	205.36		[54]
	Vacuum	KCl-$MgCl_2$-NaCl	500	1000		10		[46],[55]
	Vacuum	KCl-MgCl2-NaCl	500	1000	0.29			[53]
	Vacuum	KCl-MgCl2-NaCl	500	1000	0.36			[53]
	Vacuum	KCl-$MgCl_2$	850	100	9.8			[50]
SS 304	Argon	$MgCl_2$	750	100		562.44	15	[47]
	Argon	$MgCl_2$	750	200		377.29	14	[47]
	Argon	$MgCl_2$	750	500		157.76	58	[47]
	Argon	$MgCl_2$	750	1000		93.57	26	[47]
	Vacuum	KCl-MgCl2-NaCl	500	1000		10		[46],[55]
SS 347	Vacuum	KCl-$MgCl_2$-NaCl	500	1000		120		[46],[55]
	Vacuum	KCl-MgCl2-NaCl	500	1000	0.29			[53]
	Vacuum	KCl-MgCl2-NaCl	500	1000	0.75			[53]
Hastelloy N	Argon	KCl-$MgCl_2$-NaCl	600	400	0.41		4	[49]
	Argon	KCl-$MgCl_2$-NaCl	700	400	0.62		15	[49]
	Argon	KCl-$MgCl_2$-NaCl	800	400	1.48		36	[49]
	Vacuum	KCl-$MgCl_2$	850	100	10.7			[50]
	Vacuum	KCl-$MgCl_2$-NaCl	500	1000		50		[46],[55]

In the referenced literature, corrosion metrics are typically determined using mass change, surface area, and imaging such as scanning electron microscopy (SEM) or energy dispersive X-ray spectroscopy (EDS). Corrosion rates are reported in mg/cm^2 or μm/year. Under argon cover gas, the lowest reported corrosion was Haynes 230 at just 8 μm/year, with Inconel 625 trailing closely at 9 μm/year, both tested at 750 °C [47]. A separate study found Haynes 230 corrosion of 16.14 μm/year and Hastelloy C276 corrosion of 10.03 μm/year for 800 °C [48]. This data came

from a 2016 study in which the alloy was left in molten chloride salt for 16 days (384 hours). The Hastelloy C276 findings differ from the results of a 2018 study which found a corrosion rate of 79 μm/year at 700 °C after 500 hours [51]. However, the same study found high corrosion for Inconel 800H, 364 μm/year at 700 °C after 500 hours [51]. Similarly, Grégoire et al found 330 μm corrosion depth in Inconel 600 after 300 hours in 700 °C NaCl–KCl under argon [52]. Data in a vacuum was found for the three stainless steels [55],[46]. All were tested at 500 °C, at which SS 304 had the lowest corrosion of 9 μm/year followed by SS 316 at 10 μm/year. SS 347 showed a much higher value of 120 μm/year. At temperatures above 700 °C, SS 304 and SS 316 under argon also had high values of 377.29 μm/year and 205 μm/year, respectively [47], [54]. SS 304 and 316 had good corrosion resistance in a vacuum at 500°C, but the nickel alloys had much better resistance at higher temperature. The only exception was Hastelloy N, which was part of the same 500 °C corrosion study under vacuum as the three stainless steels [55], [46]. Hastelloy N showed 50 μm/year of corrosion, better than SS 347 but significantly higher than SS 316 or SS 304. A single data point was also found for commercially pure 99% nickel, typically referred to as Ni200 [46],[55]. This study exposed Ni200 to $MgCl_2$-NaCl salt at 520 °C for 140 hours in open air, resulting in a reported corrosion rate of 57 μm/year. Figure 1 plots some of the μm/year corrosion rates found in review, reported in Table 2, for alloy candidates in chloride salts at varying temperatures.

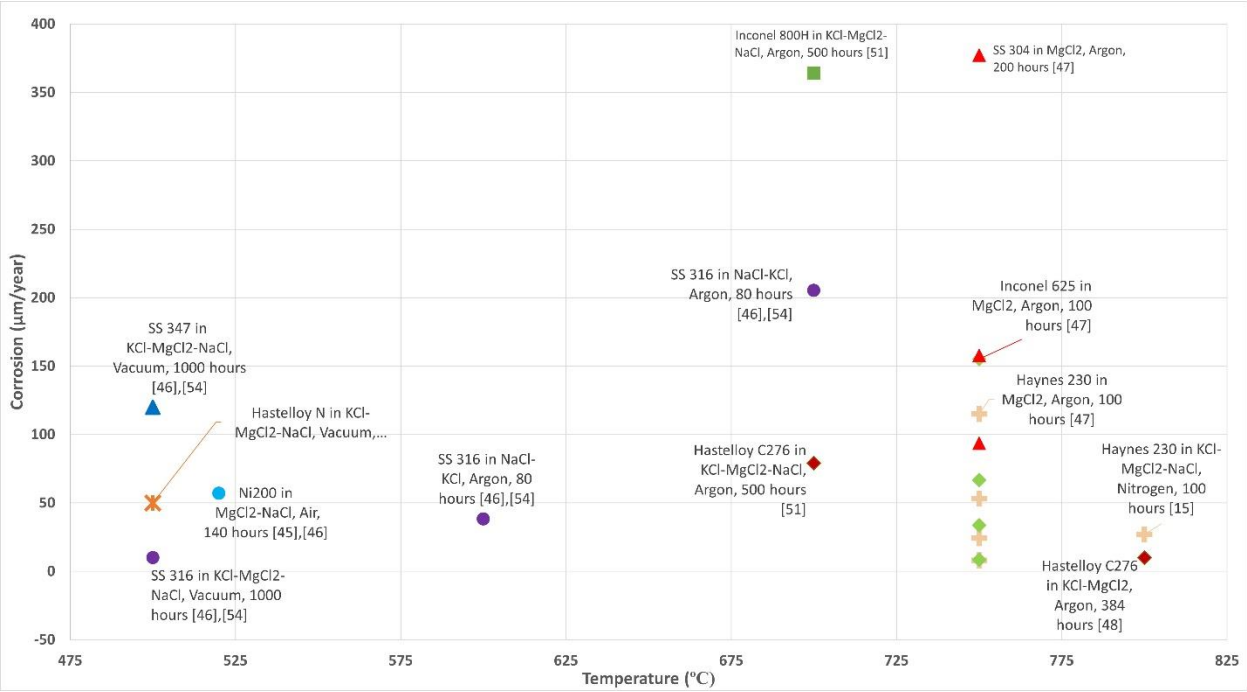

Figure 1: Corrosion of Alloys in Chloride Salt (µm/year)

Figure 2 plots some of the corrosion reported in mg/cm^2 for various alloys in molten chloride salts with temperatures between 500 °C and 850 °C. The rest of the data is reported in Table 2. The findings are similar to the corrosion data reported in Figure 1. Values at 500 °C come from Susskind et al, who reported low losses for SS 316 and 347 in a vacuum of 0.33 mg/cm^2 and 0.53 mg/cm^2, respectively [53]. Similarly, Susskind et al reported that at 500 °C in a vacuum, Inconel 600 had a low mass loss of 0.37 mg/cm^2. However, like the trends shown in Figures 1 and 2, as temperature increases few alloys maintain corrosion resistance. 2011 research by Ambrosek at 850 °C in a vacuum found that Inconel 600 and SS 316 have significant increase in mass loss, up to 14.8 mg/cm^2 and 9.8 mg/cm^2 respectively [50]. At the same temperature and under vacuum, Inconel 800H had losses of 13.1 mg/cm^2, Hastelloy N had losses of 10.7 mg/cm^2, and Haynes 230 had the lowest loss of 6.9 mg/cm^2. Research by Sun et al found that at 800 °C under argon

cover gas, Haynes 230 gained 0.26 mg/cm^2 [49]. Sun et al also found Hastelloy N and Hastelloy C276 both had a mass loss of 1.48 mg/cm^2 at 800 °C. Like the corrosion data in Figure 1, Haynes 230 and Hastelloy C276 had amongst the lowest mass losses at high temperatures. Most other alloys had high mass loss at increased temperature.

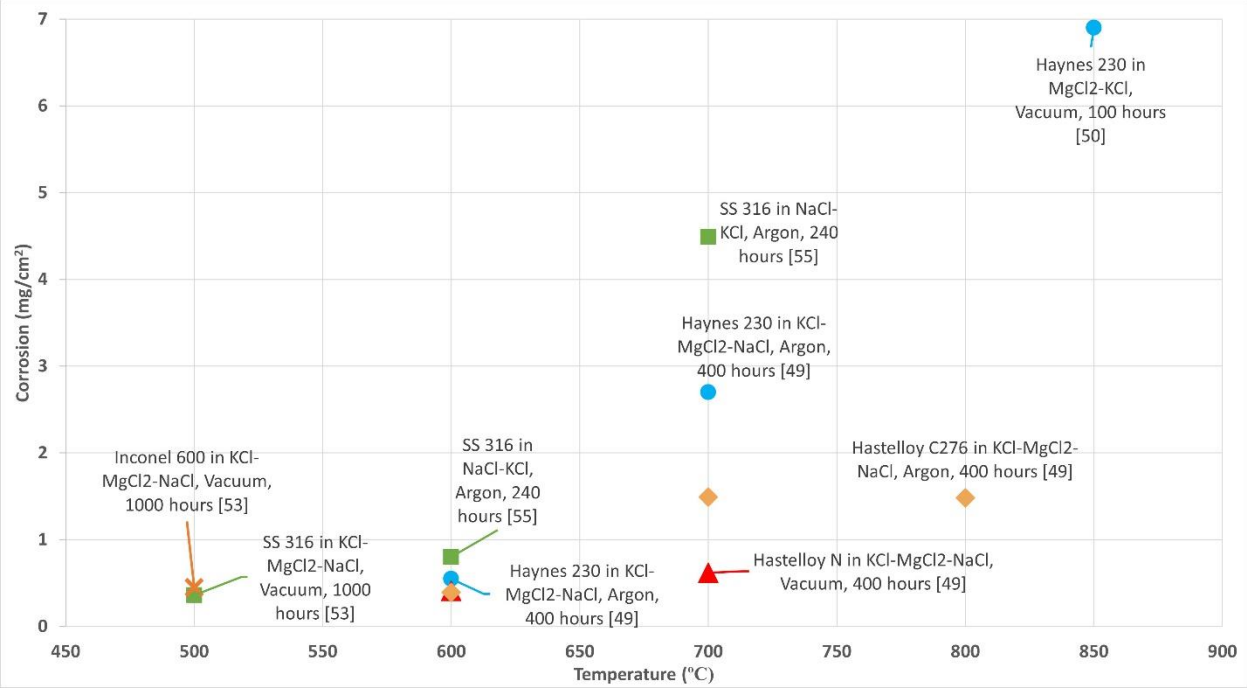

Figure 2: Corrosion of Alloys in Chloride Salt (mg/cm2)

In addition to data found for corrosion and mass loss in a vacuum or argon cover gas, some corrosion data exists for additional cover gases and test atmospheric conditions. Studies by Lai were conducted in a nitrogen environment with a small percentage of water and oxygen, with 900 °C ternary chloride salt [46],[55]. The corrosion of Haynes 230 and Inconel 800H were reported as 20345 μm/year and 23725 μm/year, respectively. SS 316 and SS 304 both reportedly disintegrated. These corrosion rates are extreme and were therefore removed from plots. The high corrosion is possibly from the water content, resulting in hydrochloric acid formation.

1.4 Discussion

Several alloys show promise for use with molten chloride salt based on the available literature. The best performance alloys at high temperature are all nickel based. Stainless steels do demonstrate good corrosion resistance in low temperature applications. SS 304 and 316 had low corrosion at 500 °C in a vacuum with values of 10 μm/year or less. Yet under an argon cover gas at higher temperatures of 750 °C, the corrosion rates are too high. Of the nickel alloys, Haynes 230 has the most available data and generally showed low corrosion under argon cover gas at 750 °C and 800 °C. The overall lowest corrosion value obtained in this review was for Haynes 230 in 750 °C $MgCl_2$. When compared to other alloys in the same conditions, Haynes 230 tends to have the lowest corrosion rates. Another Haynes product, Hastelloy C276, shows promise for chloride salt applications. Haynes International reports that Hastelloy C276 has exceptional resistance to stress corrosion cracking in chloride containing solutions, as well as resistance to chloride pitting and crevice attack [35]. Some data was found to support this claim for molten salt applications, though results are conflicting as one study found 10.03 μm/year corrosion while another found 79 μm/year. Inconel 625 had one of the lowest corrosion rates reported, 8.55 μm/year at 750 °C. However, much less corrosion data exists for Inconel 625. Only one data set on Inconel 625 could be found, sourced from a 2019 CSP HTF study in which Inconel 625 was exposed to $MgCl_2$ at 750 °C [47]. More data can be found in salts with $CaCl_2$, however $CaCl_2$ was not included in this review [56],[57]. This makes Haynes 230 and Hastelloy C276 better candidates for chloride salt applications, until more data can be produced for alloys like Inconel 625.

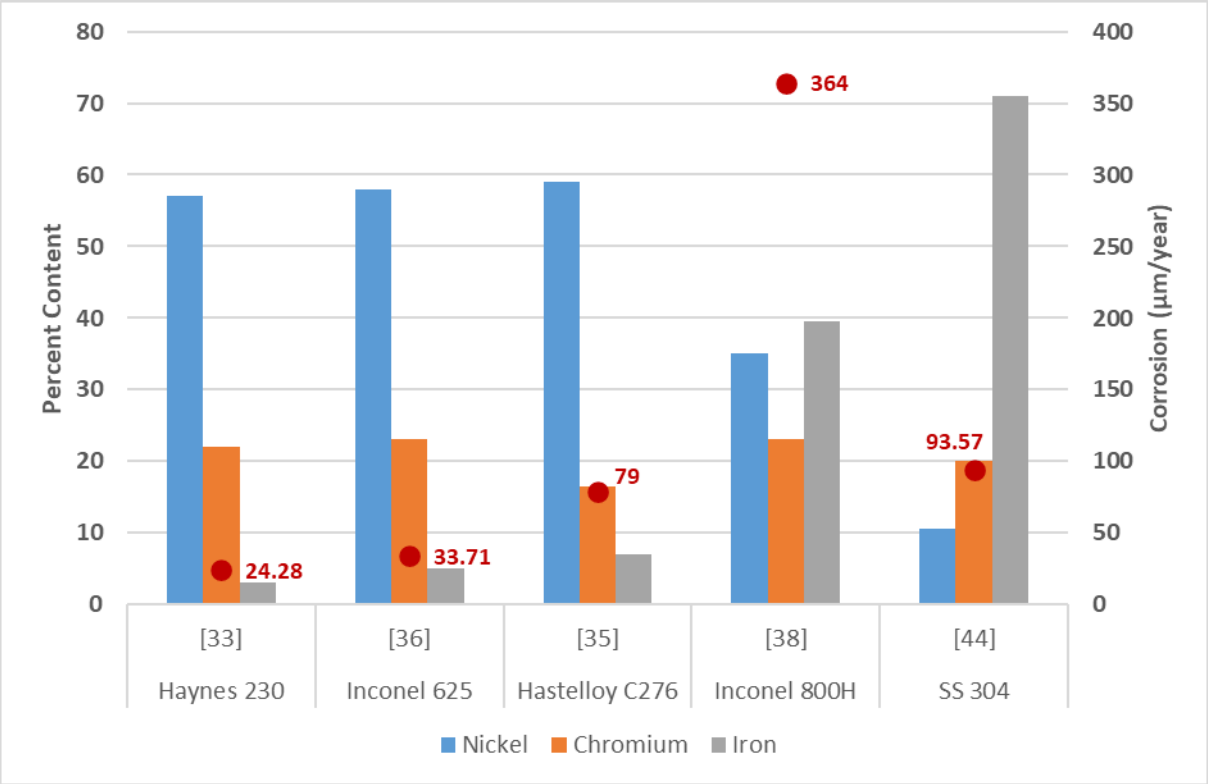

Figure 3: Alloy Composition vs. Corrosion Rate

When considering the composition, it is not surprising that alloys like Haynes 230, Hastelloy C276, and Inconel 625 have such good corrosion resistance. Figure 3 plots nickel, chromium, and iron content of some alloys considered against corrosion rates reported after 500–1000-hour exposures to 700-750ºC chloride salts. As previously discussed, iron and chromium are correlated with high corrosion in chlorides, while nickel is correlated with corrosion resistance. Haynes 230, Hastelloy C276, and Inconel 625 all have high nickel content. Inconel 800H has the lowest nickel content and highest iron content of any of researched alloys, and had reported corrosion rates of 364 µm/year at 750 °C. This was the highest corrosion rate of any nickel alloy under a vacuum or argon cover gas. The austenitic stainless steels all have low nickel content and high iron, and all three had high corrosion and mass loss rates at high

temperatures. Haynes 230, Hastelloy C276, and Inconel 625 likely outperform Inconel 800H and austenitic stainless steels due to high nickel content and low iron content. However, Inconel 600 has the highest nickel content of any alloy considered, and yet reported Inconel 600 corrosion is significant. Inconel 600 showed 200-700 μm corrosion depth in NaCl-KCl between 700-900 °C, by Salinas-Solano et al and Grégoire et al [52],[58]. One possible explanation is the presence of beneficial alloying elements. As previously mentioned Oryschich and Kostyrko [32] found that the presence of cobalt, molybdenum, and tungsten increase corrosion resistance of nickel alloys. Increased nickel content for higher dissolution of alloying elements into the metal [31]. In Haynes 230, Hastelloy C276, and Inconel 625 all have refractory metals and cobalt, while Inconel 600 has none. Similarly, Inconel 800H lacks refractory metals or cobalt.

Unfortunately, making comparisons of alloys is challenging due to availability of data. For this review, only corrosion data in the presence of binary and ternary chloride salts was collected. Though chloride salt corrosion experiments are becoming more common, it is still challenging to find high temperature corrosion data. For some of the alloys listed as of-interest, such as Inconel 740H, no non-proprietary corrosion data could be found. Furthermore, experimental methodology varies greatly between studies. Most importantly, salt chemistry differs between the papers found in this review. Temperature ranges are also not consistent between studies. Different atmospheric environments are reported, typically argon, nitrogen, open air, or vacuums. Reported corrosion rates in air are high, making it difficult to compare with corrosion under argon or a in a vacuum. Crucible materials even differ, though ceramics are most common. The purity of the salts used is also an inconsistent factor between studies. As shown by Zhao [15], salt purity can significantly impact observed corrosion rate of alloys. A

review by Raiman of previous chloride salt corrosion studies has considered this factor and established there is a connection between salt purity in published tests and reported corrosion rates [59]. Therefore, cross comparison of reported corrosion rates from the existing body of data can be challenging. Few studies have analyzed large varieties of materials, and a lack of consistent methodology between differing studies makes cross comparison scientifically flawed. If two alloys have been tested in different salt chemistries or purities, at different temperatures, with differing atmospheric conditions, containment methods, and test durations, one alloy cannot reliably be described as better than another for chloride salt applications. For reliable engineering of sensible heat storage systems with molten chloride salt, a body of cross-comparable corrosion data from consistent methodology is needed.

CHAPTER TWO: ESTABLISHMENT OF A CHLORIDE SALT CORROSION STUDY AT SANDIA NATIONAL LABORATORIES

2.1 Sandia National Laboratories Salt Corrosion Study Overview

Following the review of existing data and the determination that a large body of consistent data is needed, a salt pot corrosion study was initiated at Sandia National Laboratories (SNL). The molten salt pot corrosion project at the National Solar Thermal Test Facility (NSTTF) of SNL was an eight-part test series intended to study the viability of materials for subcomponents of valves in ternary chloride salt piping systems. The primary focus of the testing was on the previously identified nickel alloys of interest in our literature review. However, the test was expanded to over multiple test series which tested over 70 material types and hundreds of individual samples in total. The test used a sealed vessel to create an inert environment within which material samples could be submerged in 750 °C ternary chloride salt for between 500-1300 hours. The salt and samples were contained in a 1gallon alumina crucible within the test vessel. All tests used Ultra High Purity (UHP) nitrogen cover gas and purified ternary chloride salt provided by the National Renewable Energy Laboratory (NREL). The test was divided into eight different series specific to the types of materials being studied, though all tests contained the high nickel alloy Haynes 230 as a baseline for comparison. The test series are listed in the Table 3, detailing material type studied, applications of the material to valve design, and the test duration.

Table 3: Test Series Overview

Test Series #	Material Type	Valve Subcomponent	Duration
1	Nickel alloys and welded nickel alloys	Body, bonnet, plug, seat, retainer	500 hours
2	Ceramics	Guides, plugs, seats, trim parts	500 hours
3	Nickel alloy weld/filler rods	Overlay on trim parts or plug, guides, and seat	500 hours

4	Stainless steel cladded Overlays	Flow surfaces, heat pipe valve stem	500 hours
5	Compressed material, bellows sample	Valve packing and bellows	500 hours
6	Tungsten carbide ceramics and bellows sample	Valve body, seat/stem, bonnet, piping connections	500 hours
7	Coated ceramics and Haynes 230 variations	Body, bonnet, plug, seat, retainer	500 hours
8	Long duration study of down selected materials	All the above	1300 hours

2.2 Test Design

To conduct these eight tests, a system was needed capable of maintaining required temperature, pressure, salt purity, and internal atmospheric conditions. Inconsistencies in atmospheric conditions or salt purity levels could significantly affect corrosion rates on material samples. All ternary chloride salt used in this study was of the chemistry 20% NaCl/40% MgCl2/40% KCl by mol wt % and was purified by NREL. The salt was purified by pre-drying up to 250°C, purifying at 670°C with the addition of magnesium to reduce MgOHCl and other impurities, sparging with nitrogen, and then slowly cooling the salt allowing sludge to settle [15]. The resulting salt had impurity levels of approximately 0.1 wt.% of MgOHCl, less than 100ppm of sulfur, and less than 50ppm of iron [15]. 12-15lbs of salt was purified by NREL for each of the SNL corrosion tests.

Once the salt has been purified, it cannot be exposed to moisture. Impurity MgOHCl formation in the presence of water is a well-documented phenomenon with chloride salts, correlated with increased corrosion rates [15]. The hygroscopic nature of $MgCl_2$ means the presence of air can result in MgOHCl formation [15]. The introduction of air or other external moisture sources to the salt must be prevented with a perfectly sealed system and an inert cover gas. Accordingly, a test setup and salt handling procedure were devised which would maintain the purity of the salt, with assistance from the University of Wisconsin Madison. The primary

concern was jeopardizing the salt purity while shipping to SNL from NREL, transporting, and filling the corrosion salt pot. With 15lbs of purified salt, a large, sealed container would be required for shipping, vacuum purged or packaged under a glove box, and filled with cover gas to maintain positive pressure and prevent air ingress. Said container would then need to be opened and used to fill the corrosion testing salt pot before sealing, without ever allowing contact between the salt and air or any other moisture sources. As the corrosion test salt pot is over 36inches tall and weighs over 150lbs, filling in a glove box or other inert environment would be challenging, exhaustive, and potentially hazardous. Therefore, a test setup was designed using two vessels, the first of which was the corrosion test pot. The second was a salt transfer vessel specifically utilized to avoid impurities during transportation and salt filling. The transfer vessel was designed to be filled with salt, transported to SNL, and integrated into the test setup while keeping the purified salt isolated under cover gas. A flow path of tubing could then be connected between the transfer vessel and the corrosion testing pot to flow molten salt from the transfer vessel to the test pot. This way, the corrosion test pot could be filled without compromising salt purity by air exposure. The transfer vessel was constructed of a 6NPS 316 SS pipe, a ½" 316 SS end plate, and a 316SS ANSI class 150 flange socket weld flange. A spiral wound gasket was used to seal the flange. Four 316 SS ½" tubes were welded to the external side walls to act as ports for a nitrogen supply line, a vacuum line, a thermocouple probe, and inserting a ¼" tube for flowing salt out of the vessel.

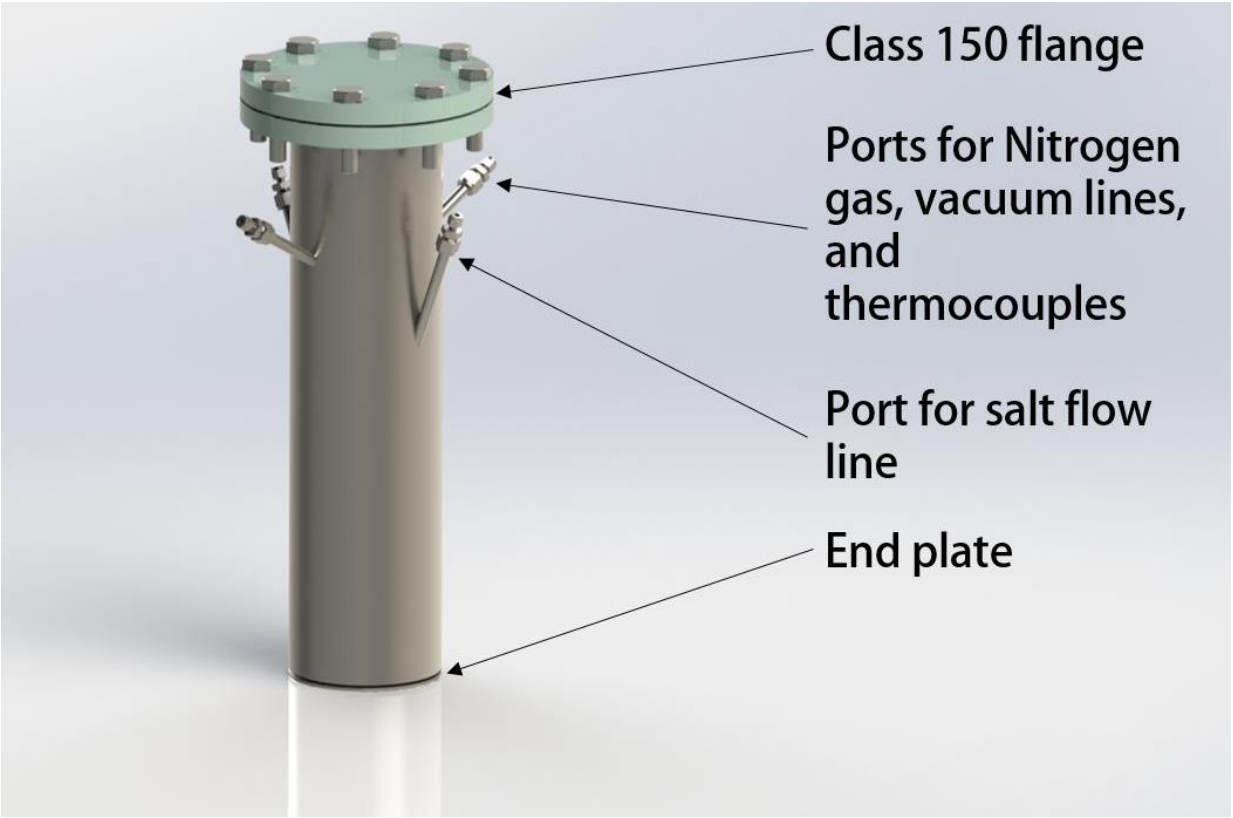

Figure 4: Transfer Vessel

Prior to each test, the transfer vessel was filled with purified salt at NREL under a glove box, filled with argon to maintain positive pressure, and shipped to SNL. The various ports on the vessel were closed with Swagelok caps for shipment. After arrival at SNL, the vessel would immediately be connected to argon cover gas supply and pressurized to maintain positive pressure while the vessel is integrated into the larger test system.

The central component of the test setup was the corrosion test pot. Actual corrosion testing was done in a 1-gallon alumina ceramic crucible. The purpose of the corrosion test pot was to create a containment vessel which could safely house the crucible and maintain desired temperature and cover gas conditions. The test pot was also constructed out of 316 SS with a 8NPS schedule 10 pipe, a ½" end plate, and a ANSI class 150 flange sealed with a spiral wound

gasket. The test pot had ports for connecting a vacuum line, a cover gas line, and for connecting the ¼" tube used to flow molten salt. There was also a ¾" port on top of the flange for a slide tube system used for raising and lowering samples into and out of the salt without exposure to air.

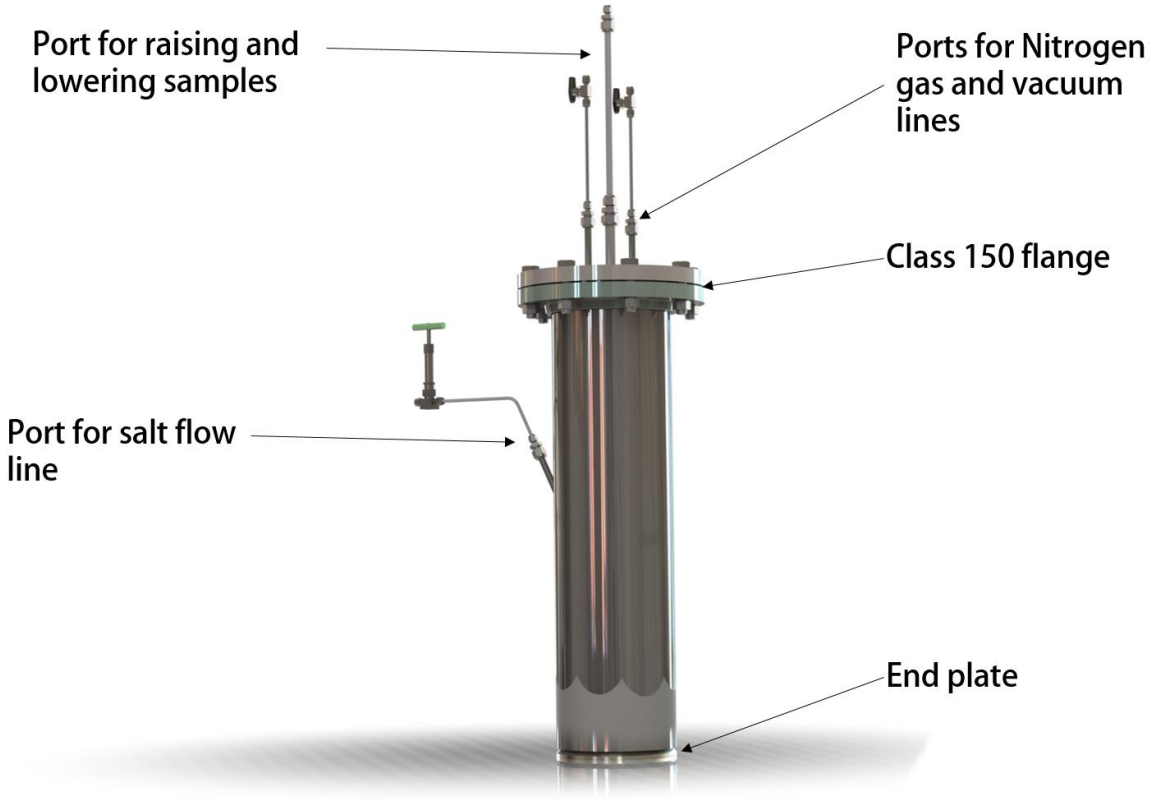

Figure 5: Salt Test Pot

As previously mentioned, to fully submerge the corrosion test samples in the molten chloride salt-filled crucible, a slide tube system was used. After filling the crucible, contained in the test pot, with salt, the test pot could not be opened to place the samples in the crucible as this would expose the salt to air. The samples could not be placed in the crucible prior to filling or left in the cooling salt after testing to be chiseled out later, as this would remove fine control of exact salt exposure time. A system for submerging and later removing the samples from the salt,

without exposure to air, was needed. Thus, a slide tube system with a plunger accessible from outside of the test pot was created. At the end of this slide tube system the material samples were hung with pure nickel wire in a series. The samples were cut into 1X1 inch square coupons, with holes drilled in the corners for the nickel wire, and spaced ½" apart.

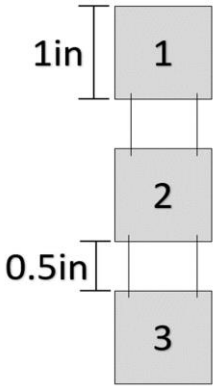

Figure 6: Coupon Sample Orientation

The strings of samples were then hung from an alumina plate, referred to as the chandelier. The samples were hung from an alumina plate to prevent galvanic coupling which could occur if two strings of samples were in contact with the same piece of metal, allowing for ion transfer. The alumina plate was a corrosion resistant and temperature rated alternative to hanging the samples from a metal hanger. Holes were drilled in the alumina plate to allow for hanging of samples in the pattern shown below.

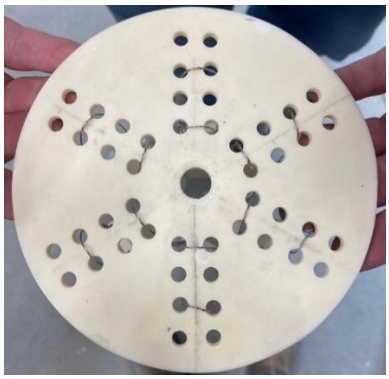

Figure 7: Alumina Disk for Hanging Samples

Pairs of holes were drilled in 6 columns, each column with 4 rows. This orientation allowed for up to 12 strings of samples to be hung from the plate. The other 12 rows were for hanging alumina spacers between rows of samples, as shown in the images below. These spacers prevented strings of dissimilar material from contacting each other, again resulting in galvanic corrosion.

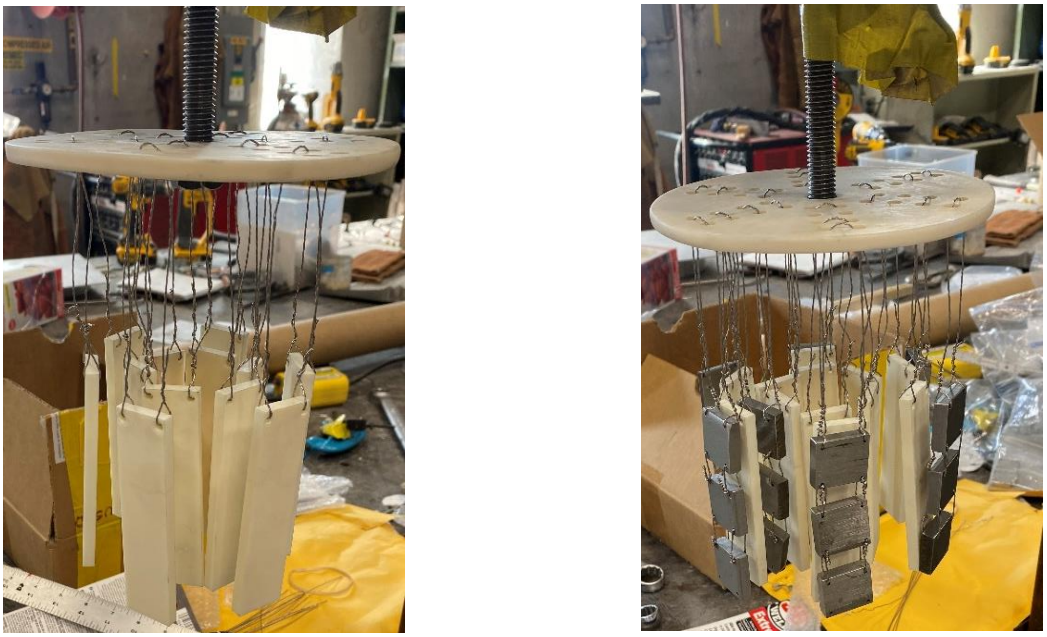

Figure 8: Coupon Sample "Chandelier" with Alumina Spacers, with and without Coupons

The alumina plate also had a 1/2” hole in the center. A threaded C276 rod passes through this hole and the alumina plate was fixed in place with a C276 nut.

Figure 9: Alumina Coupon Disk Mounted on Threaded C276 Rod

The threaded C276 segment connected to a longer ½” slide tube. To raise and lower the samples out of or into the salt-filled crucible, a previously mentioned ¾” port was placed at the center of the test pot flange. The ½” tube could slide through a 1/2”-3/4” bored through Swagelok reducing union on the port. The Swagelok fitting used Teflon ferrules which could be tightened to achieve an airtight seal on the tube or loosened to allow the tube to slide freely.

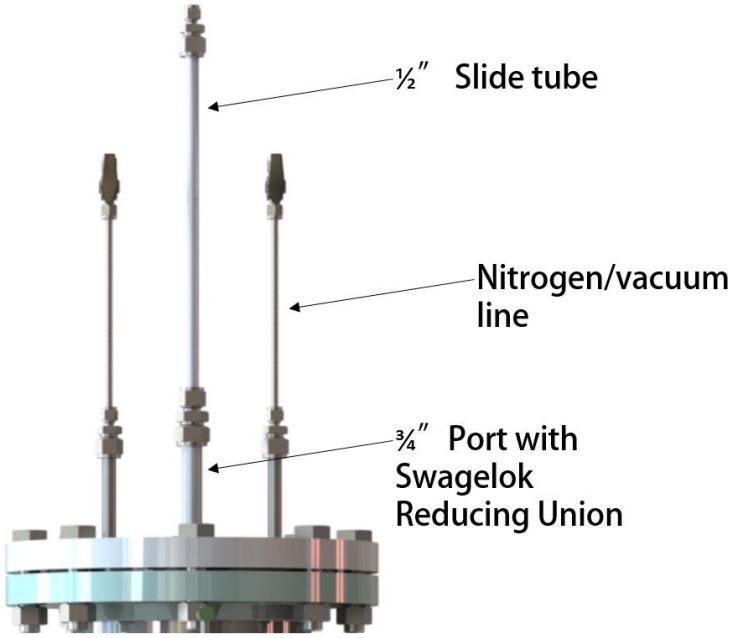

Figure 10: Top of Flange with Sliding Rod and Reducing Union

Figure 11 shows the sliding tube system, the crucible, and the sample tree chandelier outside the test pot. The tube is positioned above one of the alumina crucibles used for corrosion testing and is fixed in a makeshift stand with a Swagelok reducing union on top to allow for raising and lowering of the tube. The image shows the chandelier in the raised and lowered position. The alumina plate at the end of the slide tube is the chandelier used for hanging samples.

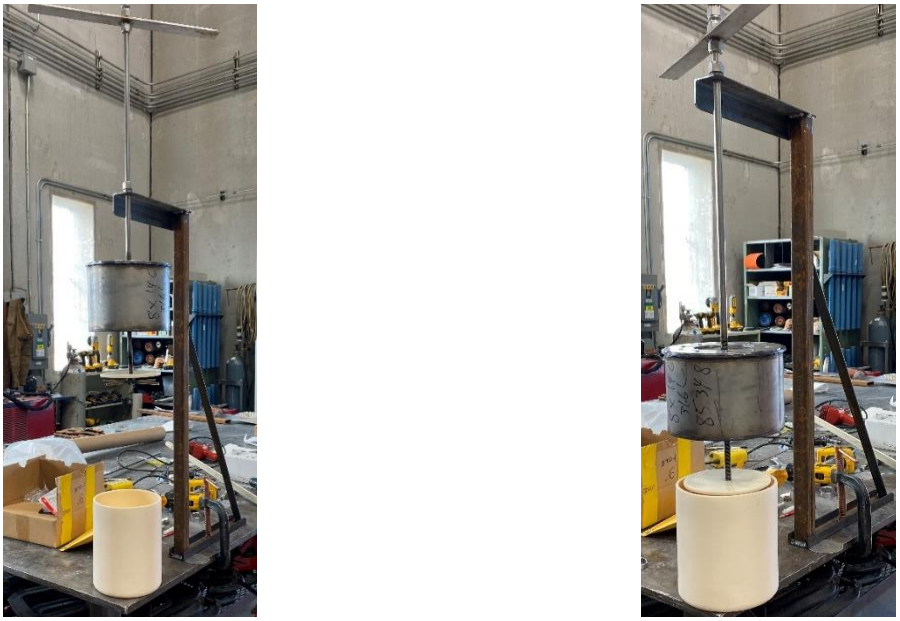

Figure 11: Sliding Rod and Coupon Holder Raised Above and Lowered into Alumina Crucible

As can be seen in Figure 11 above, there was a large metal cylinder along the length of the slide tube. This cylinder was a thermal insulator used to protect the top of the flange from test temperatures. The Teflon ferrules used in some of the fittings on the flange could only operate up to 327 °C, but the salt was to be heated to 750 °C. The system also held pressure and the flange pressure was thermally derated at test temperatures. The insulating barrier was a hollow container of 316SS, filled with Microtherm pourable insulation. It protected the flange and Teflon ferrules from the extreme temperatures at the bottom of the vessel where the salt-filled alumina crucible rested. A graphite ring at the top of the thermal barrier was used as a scrubber to maintain a tight seal between the thermal barrier and the inner diameter of the test pot.

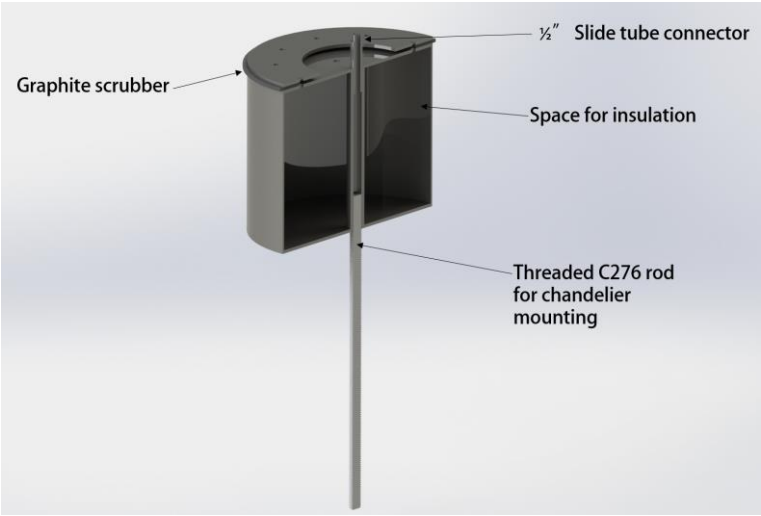

Figure 12: Thermal Insulator

The final combination of the transfer vessel, salt test pot, alumina crucible, chandelier sample holder, slide tube assembly, and thermal insulator was a system that would allow safe raising and lowering of the material samples out of and into the molten salt without exposure to air. The test pot and transfer vessel were connected by the molten salt fill line, inserted between the salt line ports on each vessel and with a Swagelok high temperature 316 SS bellows valve in between.

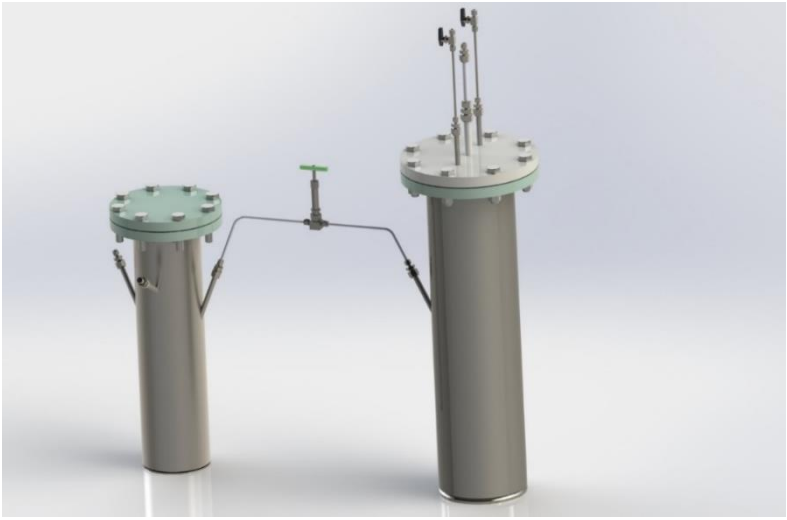

Figure 13: Complete Transfer Vessel and Test Pot Setup

Both vessels were supplied with nitrogen cover gas and had vacuum purge lines. The lines contained digital Alicat flow meters for shutting off or setting specific flow rates, pressure transducers, analog pressure gauges, PRVs, and shut off valves. To fill the test pot with salt for a corrosion test, both vessels would be heated to 500°C. The transfer vessel would be pressurized with nitrogen cover gas while vacuum was pulled on the test pot. With the test pot slide rod in the vertical position, the salt fill line connected the bottom of the transfer vessel with the bottom of the salt pot alumina crucible. The pressure and vacuum would facilitate a salt flow from the transfer vessel to the alumina crucible.

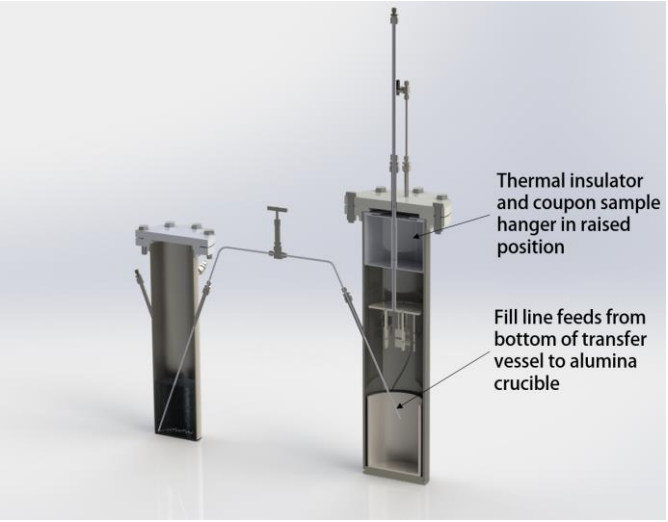

Figure 14: Cross Section of Test Setup During Salt Transfer Process (Transfer Vessel Left, Corrosion Salt Test Pot Right)

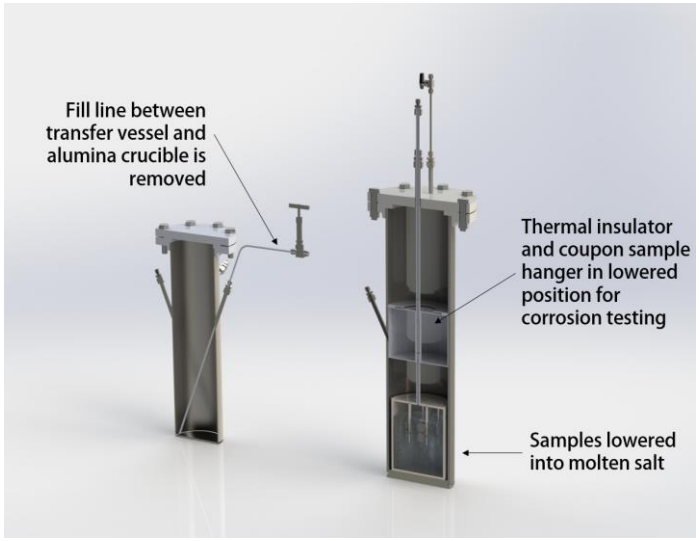

Figure 15: Cross Section of Test Setup During Corrosion Testing (Transfer Vessel Left, Corrosion Salt Test Pot Right)

The salt transfer was monitored using industrial 500lb scales placed under each vessel. The required mass of salt needed to transfer was predetermined based on the needed salt level, influenced by sample type and volume of samples in the salt. Both vessels were heated using crucible furnaces capable of 1200 °C. Each zone of each furnace has its own heat controller, allowing for highly customizable programing of ramp rates, soak times, and cool downs. All exposed components of the system, including the transfer line and upper portions of the vessels, were wrapped 120V electric heat trace. Exposed components of the vessels were only heated to ~150 °C to help mitigate thermal losses. The transfer line was heated to 550 °C to prevent formation of salt plugs during the transfer process. All components of the system were wrapped in 3 inches of insulation. Both vessels were designed and constructed following the ASME boiler pressure vessel code for welds, plate thickness, gaskets, flanges, pipe size and wall thickness, ports, tube fittings, PRVs, and pressure supplies. Approved engineering documentation exists at SNL for this system with more detailed design and engineering information.

2.3 Test Setup and Operating Procedure

Salt corrosion tests were conducted in an isolated building at the NSTTF which contains multiple test cells. These cells are small rooms for experimentation, each with a ventilation system for purging harmful gas. The transfer vessel and salt pot were placed adjacent to one another in the same test cell. External to the test cell was the UHP nitrogen and argon gas bottles, and the vacuum pump. Figure 16 below shows the overall flow diagram of the cover gas and vacuum lines used for the entire system.

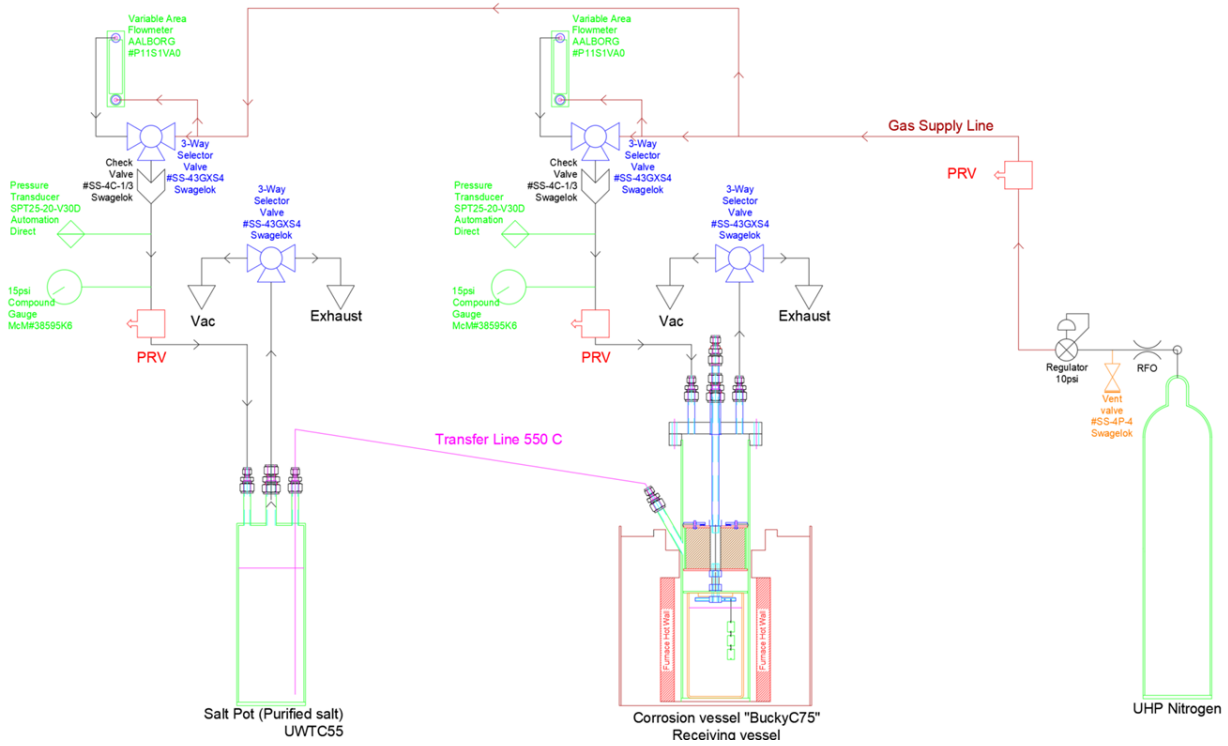

Figure 16: Corrosion Test P&ID

For each test series the procedure was the same. The only change was in the eighth test series, which ran for 1300 hours instead of 500 hours. A Technical Work Document for this project is kept at SNL which has a highly detailed procedure. The following procedure is an abbreviated version.

1. **Set Up of Instrumentation**

- The corrosion test vessel and transfer vessel were each placed in their respective furnaces, resting adjacent on 500 lb. scales. The corrosion test vessel was pre-loaded with test coupon samples. The flange was then sealed and torqued to spec.
- Furnace zones were connected to limit controllers for control of set temperatures, ramp rate, soaking time, holding times, and presetting high and low limits.
- Swagelok ports for cover gas, vacuum lines, and thermocouple insertions were connected. The ¼" transfer line was connected between the transfer vessel and salt pot.
- The transfer line and strategic exposed components were wrapped in heat trace. All components were then wrapped with 3 inches of insulation.
- Argon cover gas and a vacuum were used to cycle purge the system at least 4 times, alternating between pulling vacuum and pushing argon. Pressure transducers and PRVs were used to avoid over pressure. First, at 150 sccm, the system was pressurized to 20 psig with argon. Next, vacuum was pulled to -28 mmHg. Cover gas flow was always shut off after, never before, opening the vacuum line to avoid pulling air into the system. After cycle purging 4 times, contaminant concentration was below 0.001 ppm.

2. **Systems Check and Leak Testing**

- Using the regulator at the argon bottle, the system was pressurized to 10 psig. Systems were leak checked with detection fluid.
- At 10 psig, argon supply was cut off at the regulator. Any flow or pressure drop detected was used as indication of a leak.

- All control systems and sensors were checked for functionality.
- The argon bottle was swapped for an UHP nitrogen bottle, used for the 500-hour duration of testing.

3. Bake Out and Cycle Purge

- At this point, the furnaces and heat trace were remotely turned on, set to 250 °C.
- System was allowed to rest at 250 °C for at least 1 hour to bake out moisture.
- An initial vacuum was pulled to remove argon and moisture. All systems were then pressurized to 10 psig with UHP nitrogen.
- System was now cycled purged a second time, allowing nitrogen pressure to build to 10 psig and subsequently pulling vacuum to -28 mmHg. This was repeated 4 times to bake out and purge any moisture.

4. Salt Fill

- Temperature controllers were set to 550 °C at a ramp rate of 5 °C per minute. Slow, uniform heating of the internal salt, crucible, and vessel was necessary to avoid thermal shock damaging components. Allowing time for all components to reach matching temperatures was also critical, as contact between salt and a lower temperature component could result in freezing or thermal shock damage.
- The thermal couple probe in the transfer vessel was used to read the salt temperature. Probes on the vessels and lines were used to monitor the rest of the system.
- Once the salt temperature was 550 °C, the transfer could be initiated.
- Nitrogen flow was cut off to the corrosion salt pot and supplied to the transfer vessel only. Just 2-3 psig was needed to facilitate a transfer.

- The vacuum pump was turned on, pulling vacuum only on the corrosion salt pot, not on the transfer vessel.
- The Swagelok valve in-line between the transfer vessel and salt pot was opened when ready, initiating the transfer. The combination of nitrogen pressure on the transfer vessel and vacuum pulling on the salt pot could facilitate a consistent flow of salt between vessels.
- Transfer was monitored via the scales and the pressure gauges on the lines above each test component.
- Approximately 10 lbs. of salt were moved from the transfer vessel to the salt pot for each test.
- Transfer rate was kept slow to avoid cracking the alumina crucible.

5. Corrosion Testing Setup and Transfer Line Disconnection

- When the desired mass of salt was transferred, the valve in the transfer line was shut and any remaining salt in the line was allowed to drain back.
- A test operator with necessary PPE then disconnected the transfer line and capped the ends of the transfer line ports, isolating the salt pot for corrosion testing.

6. Corrosion Testing

- For corrosion testing, the furnaces were set to 750 °C with a ramp rate of 5 °C/min. A thermocouple probe inserted through the top of the salt pot was used to monitor the salt temperature.
- Once the salt temperature reached 750 °C, the furnace was set to soak at temperature for 500 hours.

- The coupon tree was lowered using the slide tube mechanism to submerge the samples.
- After 500 hours in the salt, the same slide tube was used to raise the samples out of the salt. The salt was allowed to cool down before removing the samples for analysis.

CHAPTER THREE: CORROSION TESTING, RESULTS, AND ANALYSIS

3.1 Testing and Results Overview

As identified in the previous corrosion literature review (Chapter One), several nickel alloys are of interest for chloride salt flow loops including Inconel 625, Inconel 800H, Haynes 230, Inconel 740H, and Haynes 282. As part of the salt pot study at the NSTTF of Sandia National Labs, all five of these alloys were subjected to ternary chloride salt (20% NaCl/40% $MgCl_2$/40% KCl by mol wt %) at 750 °C. The remainder of this paper will focus on these five alloys and the observations and findings on their compatibility with ternary chloride salt. Table 4 is a reduced version of the previous Table 1, listing the elemental composition of just these five alloys, with decreasing nickel content left to right.

Table 4: Elemental Composition of Corroded High-Nickel Alloys

	Inconel 625 [36]	**Haynes 230 [33]**	**Haynes 282 [41]**	**Inconel 740H [37]**	**Inconel 800H [38]**
Nickel	58.00 Min	57.00	57.00	37.85-52.73	30.00-35.00
Chromium	20.00-23.00	22.000	20.00	23.50-25.50	19.00-23.00
Tungsten		14.00			
Molybdenum	8.000-10.000	2.00	8.50	2.00	
Iron	5.000 Max	3.00 Max	1.50 Max	3.00	39.50
Cobalt	1.00	5.00 Max	10.00	15.00-22.00	
Copper				0.50	
Manganese	0.50	0.50	0.30 Max	1.00	
Silicon	0.50	0.40	0.15 Max	1.00	
Aluminum	0.40	0.30	1.50 Max	0.20-2.00	0.15-0.60
Titanium	0.40	0.10 Max	2.10 Max	0.50-2.50	0.15-0.60
Carbon	0.10	0.10	0.06 Max	0.01-0.08	0.10 Max
Other	3.19-4.19	0.54 Max	0.01	1.16-3.16	

To properly analyze the corrosion performance and general compatibility of these five high nickel alloys in ternary chloride salt, several metrics were used. These include visual observations, mass change of samples by corrosion, calculated corrosion rates in μm/year, calculated corrosion rates in mg/cm^2, Scanning Electron Microscopy (SEM) for high magnification imaging, Energy Dispersive X-Ray Spectroscopy (EDS) element mapping of sample surfaces, and EDS element line scanning of cut and polished sample faces.

3.2 Corrosion Rates and Mass Loss

For corrosion testing of the five nickel alloys, three coupon-type samples of each material were used, suspended in chains with pure nickel wire.

Figure 17: Pre-Test Nickel Alloy Samples left to right: Haynes 230, Haynes 282, Inconel 740H, Inconel 625, Inconel 800H

The samples were individually weighed prior to corrosion testing. After 500 hours of submersion in salt, the samples were removed and cleaned under a glove box using deionized water in an ultrasonic bath. All samples were then imaged, with some of the images shown in Figure 18.

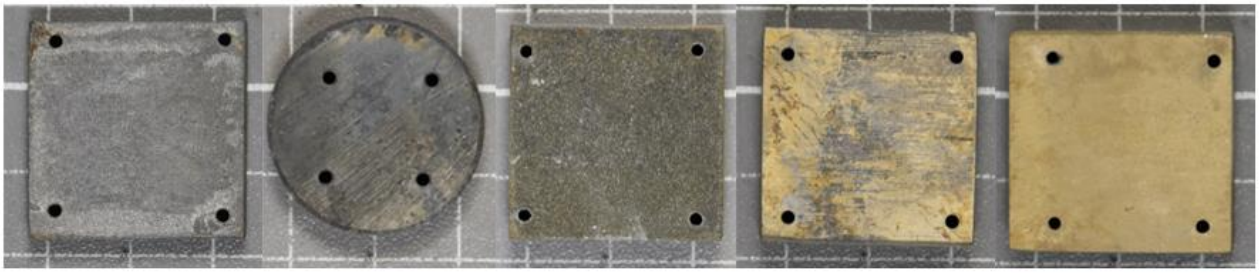

Figure 18: Post-Test, salt exposed samples left to right: Haynes 230, Haynes 282, Inconel 740H, Inconel 625, Inconel 800H

After cleaning, the samples were subsequently weighed a second time. Mass change is a primary indicator of corrosion and a useful metric for determining material characteristics in the presence of a corrosive. Tables 5-7 detail the mass data of the samples pre and post salt exposure.

Table 5: Sample Weight (Pre-Test)

Alloy Type	Sample 1 Mass (grams)	Sample 2 Mass (grams)	Sample 3 Mass (grams)
Inconel 625	35.9586	35.1802	35.6901
Inconel 800H	35.2656	34.2379	35.0777
Haynes 230	18.0427	17.7475	18.4035
Inconel 740H	36.7177	35.729	35.956
Haynes 282	12.7779	11.8516	17.2241

Table 6: Sample Weight (Post-Test)

Alloy Type	Sample 1 Mass (grams)	Sample 2 Mass (grams)	Sample 3 Mass (grams)
Inconel 625	35.9051	35.1356	35.6486
Inconel 800H	34.2964	33.3429	34.2932
Haynes 230	18.0342	17.7427	18.3907
Inconel 740H	36.8496	35.8752	36.1931
Haynes 282	12.7282	11.8137	17.1837

Table 7: Delta Sample Weight

Alloy Type	Sample 1 Mass (grams)	Sample 2 Mass (grams)	Sample 3 Mass (grams)
Inconel 625	-0.0535	-0.0446	-0.0415
Inconel 800H	-0.9692	-0.895	-0.7845
Haynes 230	-0.0085	-0.0048	-0.0128

Inconel 740H	+0.1319	+0.1462	+0.2371
Haynes 282	-0.0497	-0.0379	-0.0404

All samples in this test lost mass except for Inconel 740H, for which all samples gained mass, a phenomenon which will be evaluated further. Overall, the lowest mass loss was in Haynes 230, with an average percentage loss of 0.05%. The most significant loss was in Inconel 800H, which lost over 2.5%.

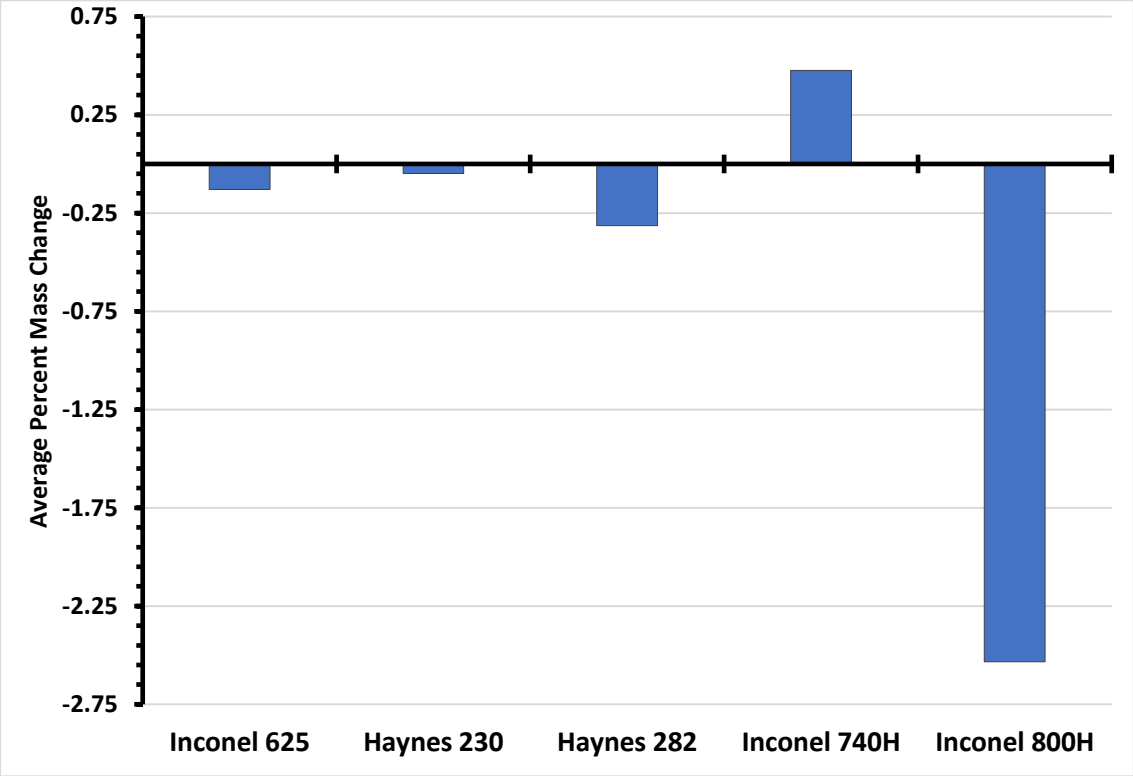

Figure 19: Average Percent Mass Change of Alloys After 500 hours of Molten Chloride Salt Exposure

After the change in mass was determined by subtracting the initial weight from the final weight, the corrosion rate was calculated based on the sample mass loss and sample geometry. This was calculated using the standard equation for corrosion shown in *equation 1*. This equation comes from the ASTM Standard Guide for Laboratory Immersion Corrosion Testing of Metals

[60]. In this equation, D is the material density, W is the change in sample weight, A is the surface area of the sample, and T is the exposure time.

$$Corrosion = \left(\frac{W}{DAT}\right) \qquad (1)$$

In this study, mass loss was measured in grams, surface area in centimeters, and the test duration was 500 hours. In *equation 1*, this gives a corrosion rate of cm/hour. To convert to the standard corrosion unit system of μm/year, *equation 2* was used.

$$Corrosion\ \left(\frac{\mu m}{year}\right) = \left(\frac{W\ (grams)}{D\left(\frac{grams}{cm^3}\right) * A\ (cm^2) * T\ (hours)}\right) * \frac{8760\ hours}{year} * \frac{10000\ \mu m}{cm} \qquad (2)$$

Another standard metric and unit system for reporting rate of corrosion is to divide the sample mass change by the sample surface area, giving a value in mg/cm^2. Tables 8 and 9 report the calculated corrosion rates for the five nickel alloys in this test, in units of μm/year and mg/cm^2.

Table 8: Corrosion Loss (μm/year)

Alloy Type	Sample 1 (μm/year)	Sample 2 (μm/year)	Sample 3 (μm/year)
Inconel 625	-55.1745	-47.0137	-43.1209
Inconel 800H	-1019.1771	-969.4010	-829.3720
Haynes 230	-10.4823	-6.0179	-15.4756
Inconel 740H	+133.2161	+151.7449	+244.5388
Haynes 282	-86.5437	-71.1543	-52.1896

Table 9: Sample Loss (mg/cm^2)

Alloy Type	Sample 1 (mg/cm^2)	Sample 2 (mg/cm^2)	Sample 3 (mg/cm^2)
Inconel 625	-2.7642	-2.3043	-2.1442
Inconel 800H	-50.0754	-46.2418	-40.5326
Haynes 230	-0.5270	-0.2976	-0.7936
Inconel 740H	+6.8148	+7.5537	+12.2502
Haynes 282	-3.9304	-2.9972	-3.1949

Of the five nickel alloys, Haynes 230 had the best corrosion resistance. Haynes 230 had an average loss of 10.66 μm/year with a 9.46 μm/year range between samples and a standard deviation of 3.86 μm/year. Inconel 625 also performed well though not as resistant as Haynes 230, showing an average corrosion rate of 48.45 μm/year with a range of 12.05 μm/year and a standard deviation of 5.02 μm/year. The other samples showed behavior outside of what could be considered acceptable for use in full scale TES systems, because of variability between samples and overall corrosive behavior. Haynes 282 samples had an average corrosion rate of 70.00 μm/year, with a range of 34.35 μm/year and a standard deviation of 14.05 μm/year. Inconel 800H had the worst performance, with an average corrosion rate of 939.32 μm/year, a range of 189.81 μm/year, and a standard deviation of 80.35 μm/year. Inconel 740H did not lose material, but instead gained an average of 176.50 μm/year, with a range of 111.32 μm/year and a standard deviation of 48.70 μm/year. This observation would perhaps be considered an outlier, but all three samples gained mass. None of the other alloys had a single sample gain mass.

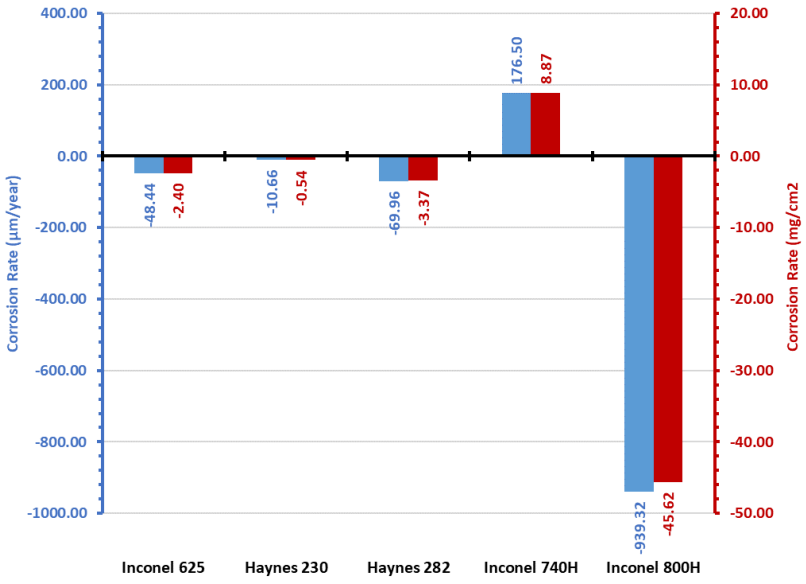

Figure 20: Average Corrosion of Alloys in 750°C Ternary Chloride Salt After 500 hours

3.3 SEM/EDS

3.3.1 General Observations and Surface Analysis

In addition to mass loss evaluation, corrosion of all five alloys was qualified by analysis of coupon samples under a Tescan Scanning Electron Microscope (SEM) for high magnification imaging and Energy Dispersive X-Ray Spectroscopy (EDS). SEM and EDS analysis was first performed on coupon sample exterior surfaces that were in direct contact with the salt, after removal from the salt and cleaning. Several alloys had developed a brittle, green patina over the exterior surfaces that required investigation. Others also showed indicators of corrosion, both visually and through surface level element composition. Initial analysis indicated that the patina was rich in magnesium and oxygen, but not sodium, potassium, or chloride components of the molten salt. It has been postulated that the magnesium reduced to an oxide or hydroxide overlayer on some coupons. The patina was identified on all five nickel alloys, though Inconel 625 and Inconel 800H only had small deposits while other alloys were evenly coated. Many microscopy images and EDS element maps were created for each coupon sample from the five nickel alloys. Only a small number of quality example images and scans are included here, but observations and statements made are based on the analysis of all collective images and data.

Inconel 800H was imaged first using the Tescan microscope and EDAX TEAM software for EDS analysis. Figures 21 and 22 show the SEM and EDS images of the Inconel 800H exterior surface. SEM images at a high magnification seem to show extreme pitting corrosion of the sample surface. EDS element mapping results primarily show iron and nickel in 48% and 29%, respectively. Chromium content at the surface was very low, indicating chromium depletion. Considering the pitting shown via microscopy and the potential chromium depletion,

initial surface analysis indicates that Inconel 800H performed poorly and was corroded by the chloride salt.

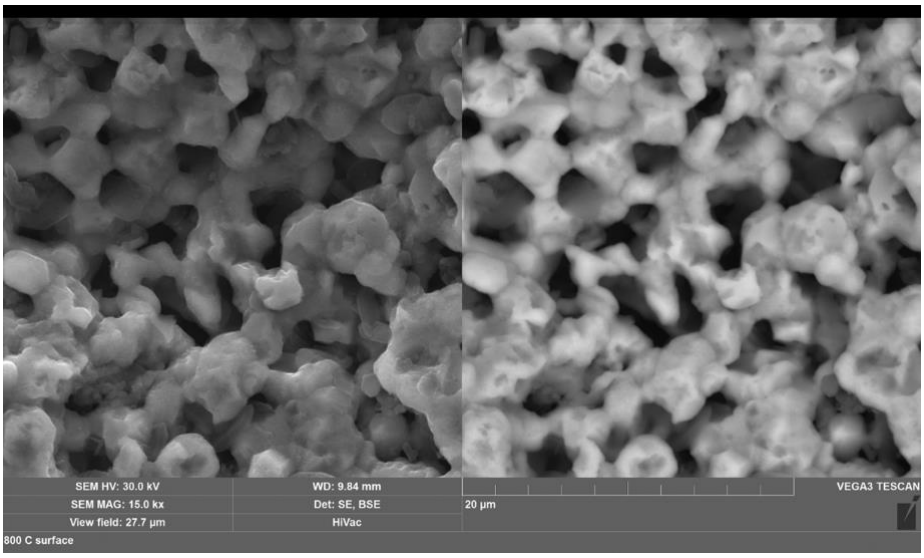

Figure 21: SEM Image of Inconel 800H

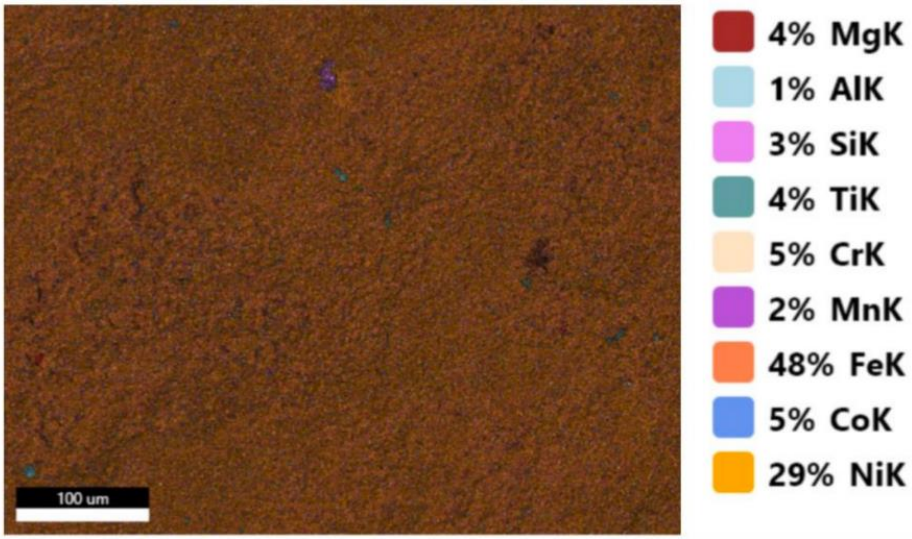

Figure 22: EDS layered scan of Inconel 800H

Next, Haynes 230 samples were image and analyzed with the Tescan Microscope. However, before all samples could be imaged, the EDS equipment failed and required replacement. An Oxford Instruments Aztec EDS imaging system and complimentary software

was integrated into the existing Tescan Vega3 microscope and subsequently used to analyze the remaining samples of Inconel 625, Inconel 740H, Haynes 282, and Haynes 230.

The Haynes 230 exterior surfaces were imaged at 100 μm magnifications. The findings suggest that H230 may have performed well. Analysis on the first two samples showed little evidence of corrosion, with a consistent content of iron, nickel, and chromium at the surface and only small evidence of salt residue.

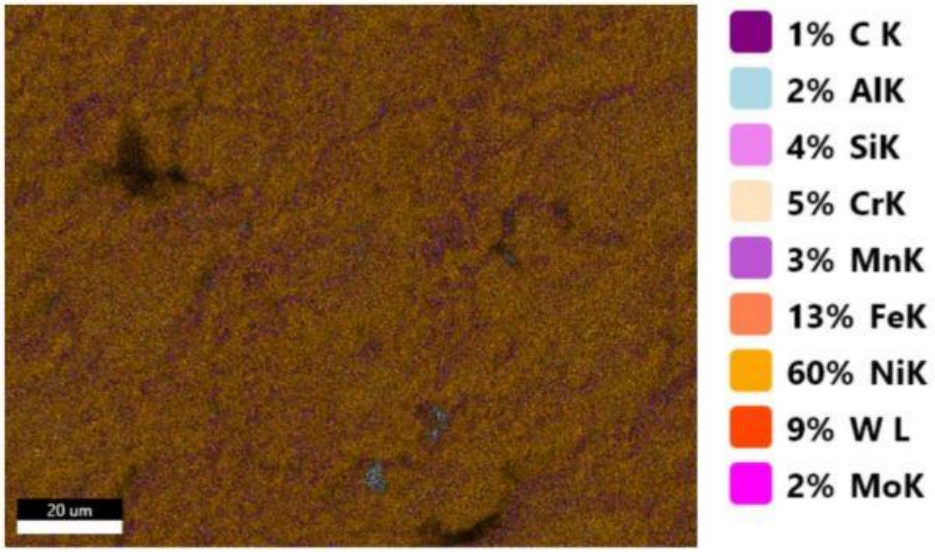

Figure 23: EDS layered scan of Haynes 230

However, the third sample, imaged with the replacement EDS equipment, showed a significant amount of salt residue. EDS analysis revealed the salt residue was almost completely magnesium oxide. The magnesium oxide did not contain any dissolved alloying elements from the Haynes 230 sample, such as nickel or chromium. It was a layer of pure salt that deposited on the sample surface. The lack of incorporated alloying elements in the salt residue further suggests that the Haynes 230 material had good corrosion resistance. However, it is unclear why such a significant amount of salt was adhered to the sample surface even after multiple washes.

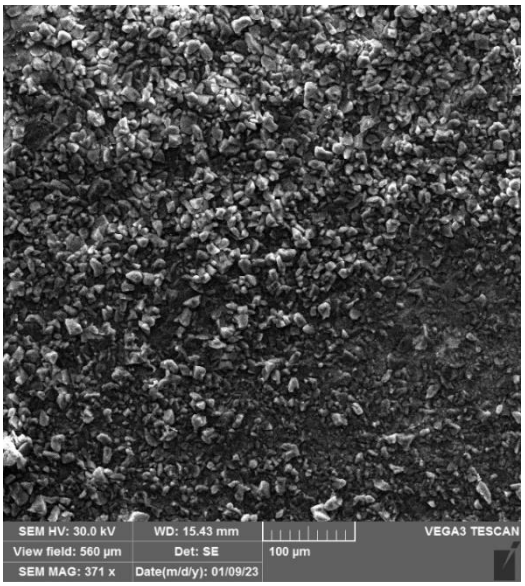

Figure 24: SEM 100 µm magnification surface image of Haynes 282

Figure 25: EDS layered scan of Haynes 230

Next, Inconel 625 sample exterior surfaces were imaged at 100 µm magnifications. The surface analysis suggested that Inconel 625 performed well in the presence of molten chloride salt over the 500-hour duration. Evenly distributed across the sample surface were the primary detected elements iron and nickel, with a significant amount of surface level chromium showing as well. No unusual distributions of alloying elements or significant depletions of chromium

were detected. These results indicate that Inconel 625 performed well. Some magnesium oxide from salt deposits remains on the surface. However, the amount of detectable surface level magnesium oxide is low compared to other nickel alloys in this test.

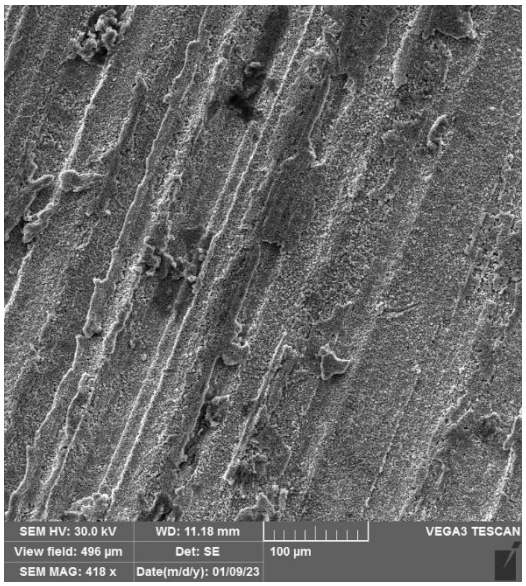

Figure 26: SEM 100 µm magnification surface image of Inconel 625

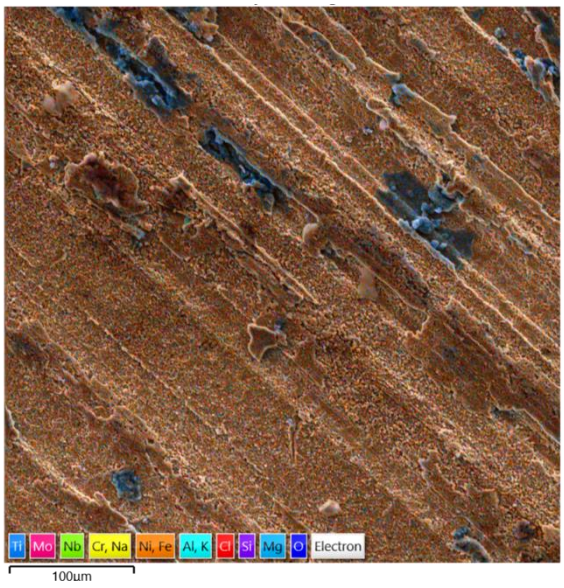

Figure 27: EDS layered scan of Inconel 625

Inconel 740H sample exterior surfaces were imaged next at 100 µm magnifications. Evenly distributed across sample surfaces, visible in both SEM and EDS, was a coating of salt

residue. This salt residue was left even after cleaning the samples with deionized water in a sonic bath. EDS revealed the salt residue was composed of magnesium and oxygen. Mixed with the magnesium oxide residue was iron and nickel. Almost 100% of the detected surface level elements were magnesium and oxygen with incorporated iron, nickel, and chromium. The alloying elements likely depleted from the Inconel 740H as a result of corrosion and reprecipitated on the sample surfaces in the salt residue. The presence of reprecipitated iron and nickel was possibly why the residue stuck to the sample surfaces rather than washing away.

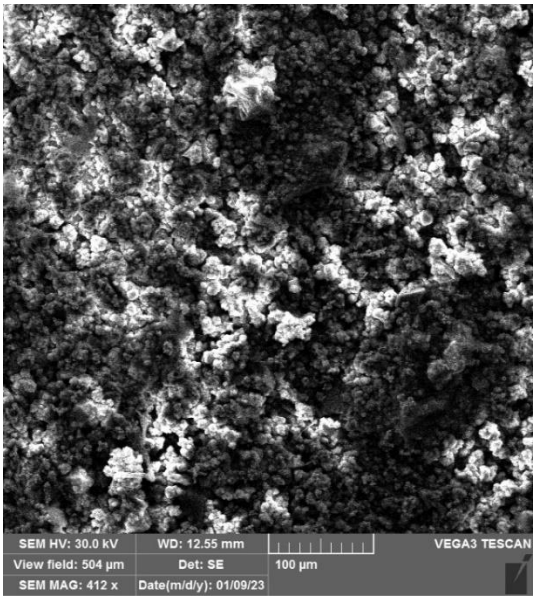

Figure 28: SEM 100 µm magnification surface image of Inconel 740H

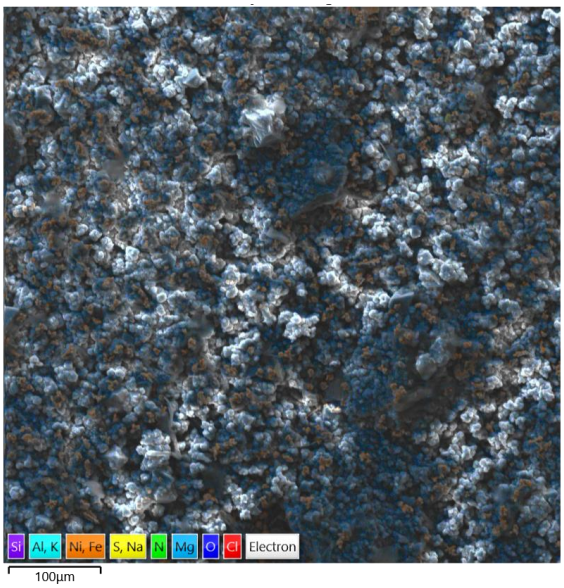

Figure 29: EDS layered scan of Inconel 740H

Finally, Haynes 282 sample exterior surfaces were imaged at 100 µm magnifications. Unevenly distributed across sample surfaces was small groupings of salt residue, however this residue was different than that found on Inconel 740H. EDS reveals the salt residue was composed of magnesium and oxygen with small amounts of sodium and potassium. The magnesium was evenly distributed about most of the Haynes 282. This may have been a result of salt and reprecipitated alloying elements forming an amorphous mix adhered to sample surfaces, like what occurred with Inconel 740H. However, there was not many areas in the EDS maps where alloying elements were clearly incorporated salt residue. Nor was depletion of chromium or other alloying elements detected at the surface. However, there was a heavy layer of aluminum mixed with magnesium at the surface, especially in one particular sample. This was only seen in Haynes 282, a layer of aluminum on a sample surface post-corrosion was not seen with the other nickel alloys. Haynes 282 also had the highest aluminum content of any nickel alloy tested in this study. It is possible that the aluminum was depleted out of the sample as a corrosion mechanism and reprecipitated in a layer of salt.

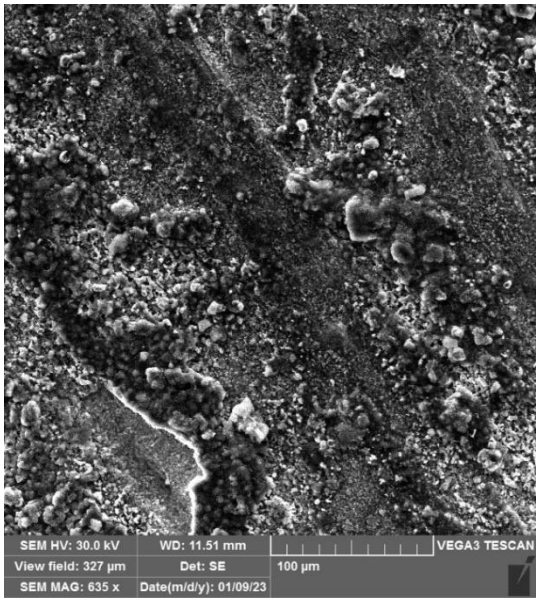

Figure 30: SEM 100 µm magnification surface image of Haynes 282

Figure 31: EDS layered scan of Haynes 282

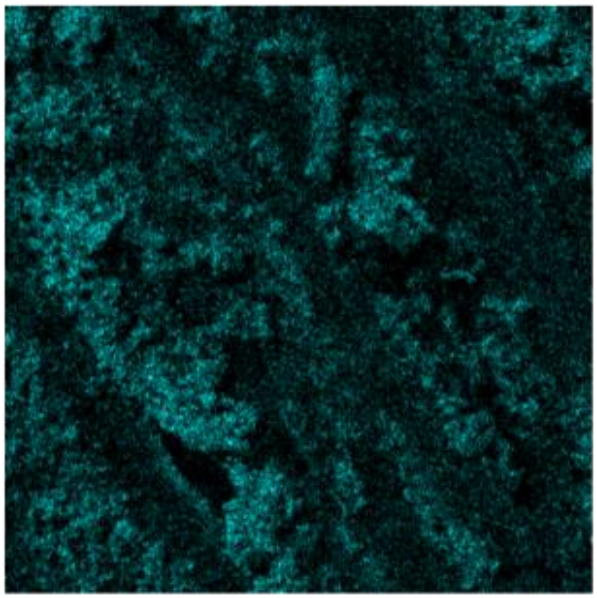

Figure 32: EDS Map of Aluminum on Haynes 282 Sample Surface

3.3.2 Chromium Depletion and Cross Section Analysis

After imaging the exterior surfaces of the nickel alloy coupons, the samples were cut and polished for EDS line scans. In this method, the elemental composition of a sample is analyzed along a straight line with user-defined start and end points, rather than across the entire visible sample. When performed on the cross-sectional face of a sample that has been cut open, a line scan shows how the elemental composition of a material varies from the inside to the exterior surfaces. For samples that have been corroded, this means useful data on what elements were depleted from the material and what the depth of depletion was. The nickel alloy samples were all cut in half, and the cut face exposing the sample cross section was polished with sandpaper on a polishing wheel from 60-1200grit. The samples were cleaned via sonicating after polishing to remove any polishing byproduct. The cut faces were then analyzed via line scan EDS. Most line scans showed visible depth of corrosion. As previously mentioned, depletion of chromium is

often a powerful indicator of nickel alloy corrosion in chloride salt [15],[23],[24],[32]. In all samples analyzed, corrosion was clearly indicated by chromium depletion.

The first cut and polished samples analyzed were of Inconel 800H, shown in Figures 33-36, which show the data from two different EDS imaging procedures. Prior to performing any EDS analysis, clear pitting corrosion was already evident. As can be seen in Figures 33 and 35, significant holes from pitting corrosion were visible from the sample exterior edge down into the sample body. EDS analysis confirmed the pitting was the result of chromium depletion. As can be seen in the line scans taken from the exterior edges into the sample bodies, the chromium content was directly correlated with the visible pitting. At the sample interior chromium, iron, and nickel content levels were all normal. But approaching the exterior edge where the pitting becomes visible, chromium content decreased sharply. This pitting and chromium depletion occurred 200-225 μm into the sample over the 500-hour salt exposure period.

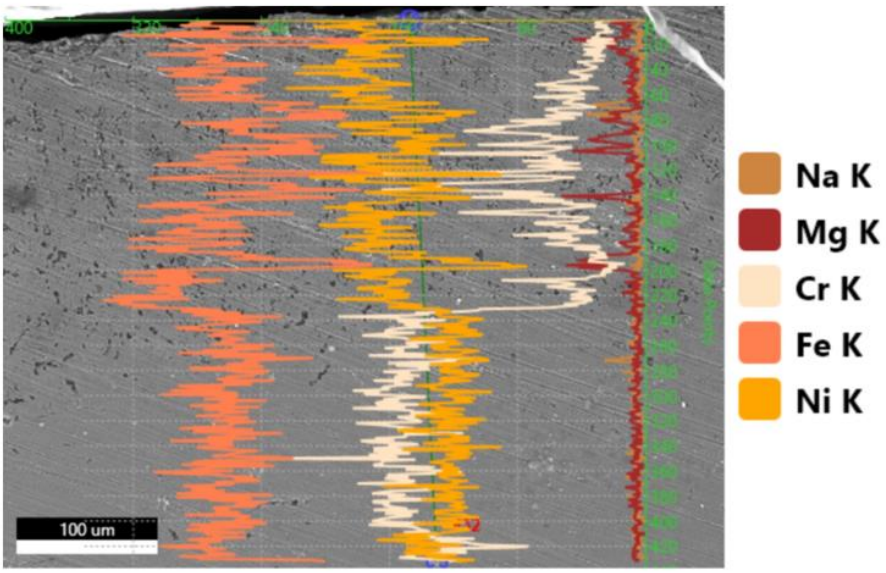

Figure 33: Cross Section EDS Line Scan of Cut Inconel 800H Area 1

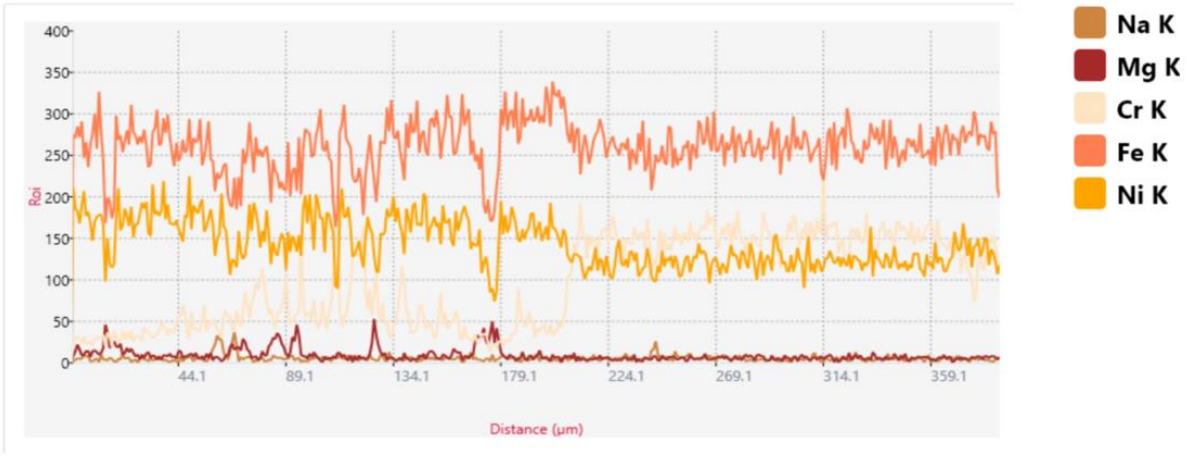

Figure 34: Element Map for Cross Section EDS Line Scan of Cut Inconel 800H Area 1

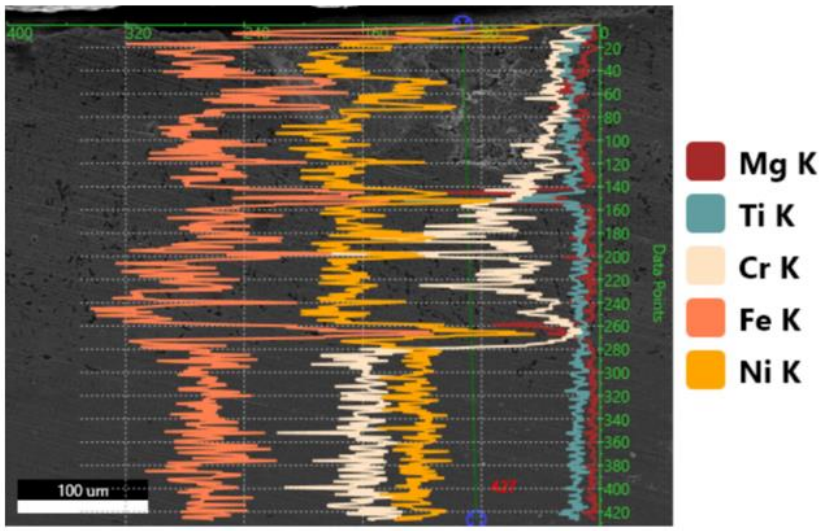

Figure 35: Cross Section EDS Line Scan of Cut Inconel 800H Area 2

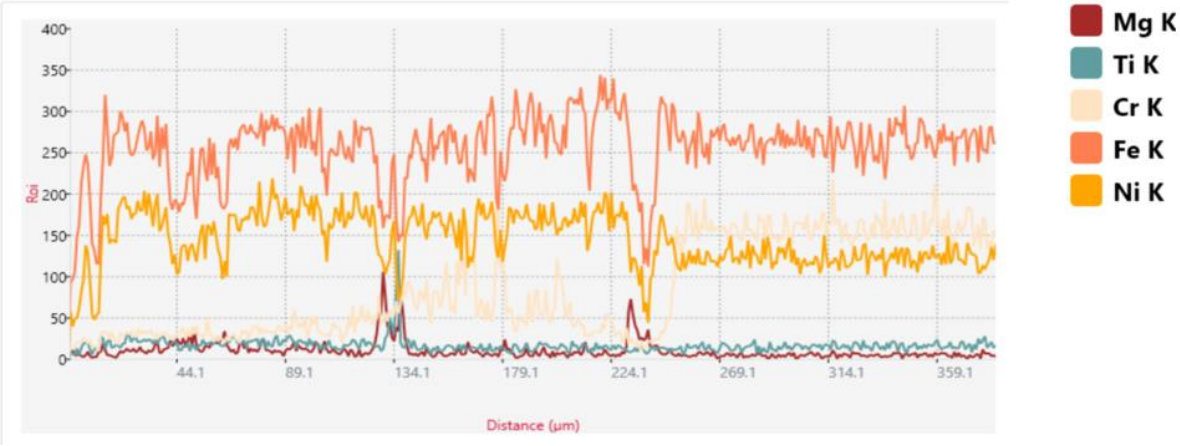

Figure 36: Element Map for Cross Section EDS Line Scan of Cut Inconel 800H Area 2

Next, Figures 37-40 provide data from EDS line scan analysis on the cross-section cut faces of Haynes 230 samples. These scans were done at a higher magnification than the previous Inconel 800H imaging as the depth of corrosion was not nearly as extreme. Immediately obvious was the tooling marks on the cut surface, indicating that the polishing quality was not high. However, corrosion analysis was still easily performed with the data obtained. As can be seen in the EDS line scan images Figures 37 and 39, there was some pitting corrosion near the edge of the Haynes 230 samples, in the first ~30 μm from the edge. However, the pitting was not nearly extreme as was seen with Inconel 800H. The worst of the pitting damage was in the first ~10 μm. Pitting on the Haynes 230 sample surface directly correlated with changes in elemental composition. EDS data shows that chromium depletion occurred in the first 20-30 μm along with increased iron content, corresponding with the visible pitting. There was no appreciable change in nickel content in these scans. This analysis clearly indicated corrosion damage through the first 30 μm of Haynes 230, but not further.

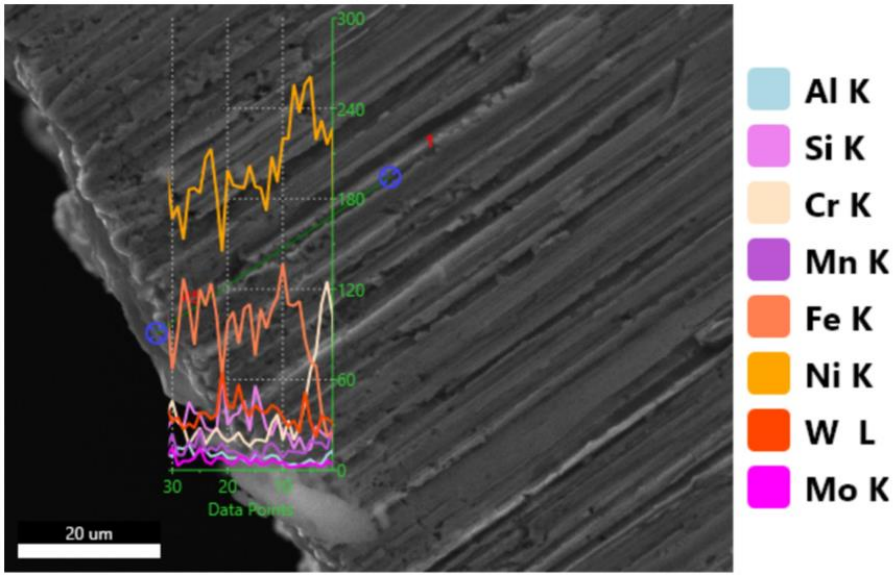

Figure 37: Cross Section EDS Line Scan on Cut Face of H230 Area 1

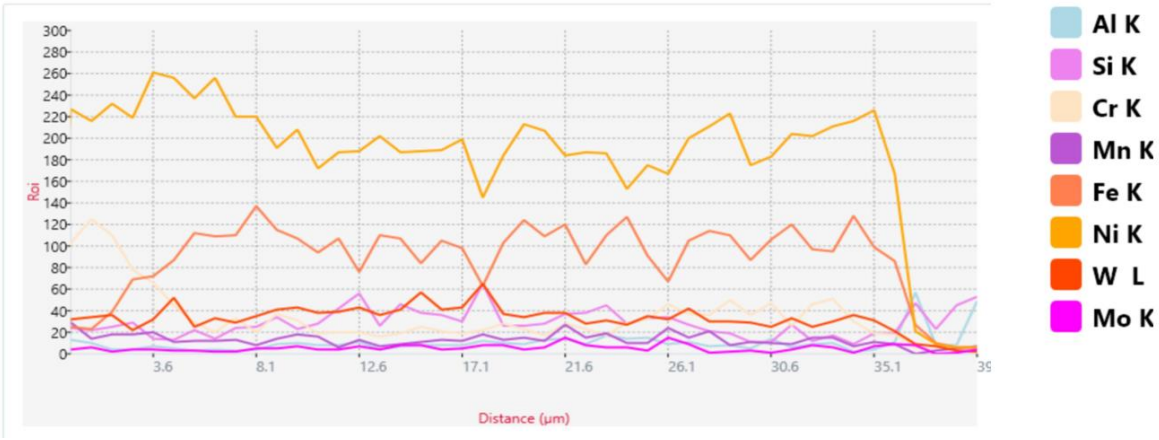

Figure 38: Element Map for Cross Section EDS Line Scan on Cut Face of H230 Area 1

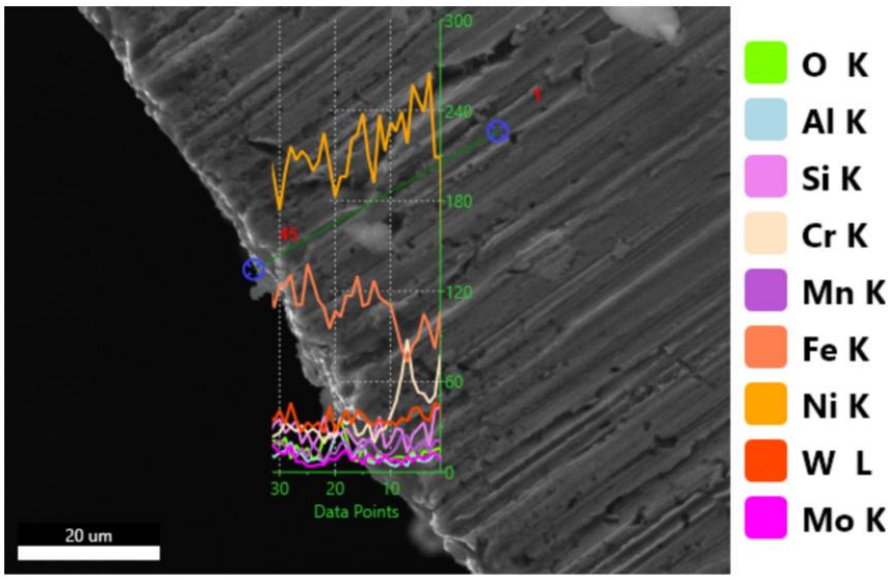

Figure 39: Cross Section EDS Line Scan on Cut Face of H230 Area 2

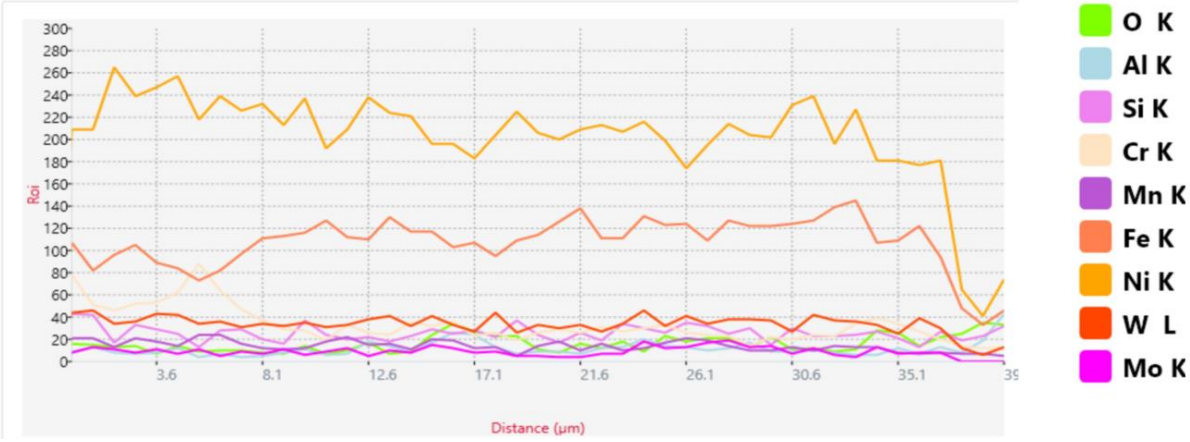

Figure 40: Element Map for Cross Section EDS Line Scan on Cut Face of H230 Area 2

Figures 41-44 show results from EDS line scan analysis on the cross-sectional faces of Inconel 625 samples. Very little pitting corrosion could be seen on these sample surfaces, even at the 20 μm scale. Some possible pitting could be found, but overall there was little visual evidence of corrosion. The only evidence of corrosion was found in the EDS elemental composition imaging. From the exterior edges of the samples to an approximate 20-30 μm depth, there was chromium depletion and increased iron content. Nickel content held consistent throughout the length of the line scan. The data provided by this analysis suggests that Inconel 625 performed well over the 500 hour duration submerged in molten chloride salt.

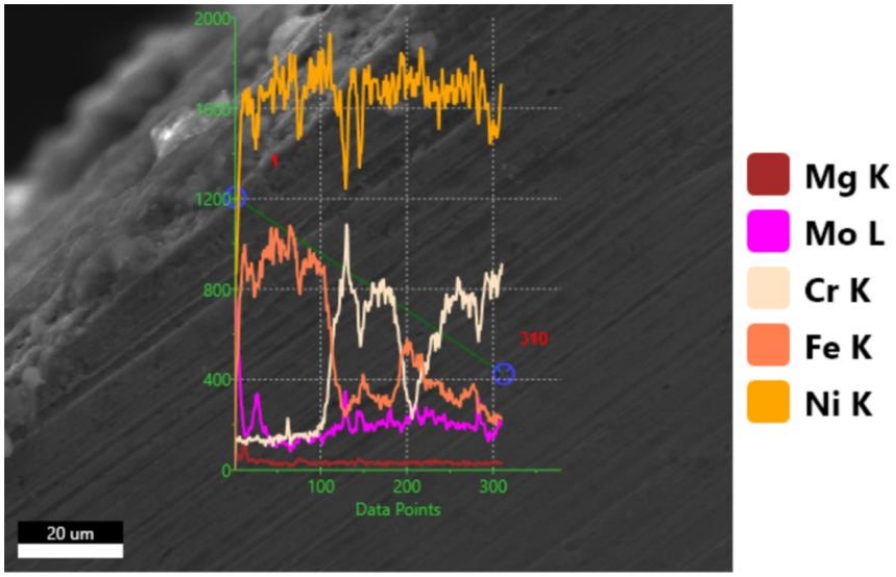

Figure 41: Cross Section EDS Line Scan of Cut Inconel 625 Area 1

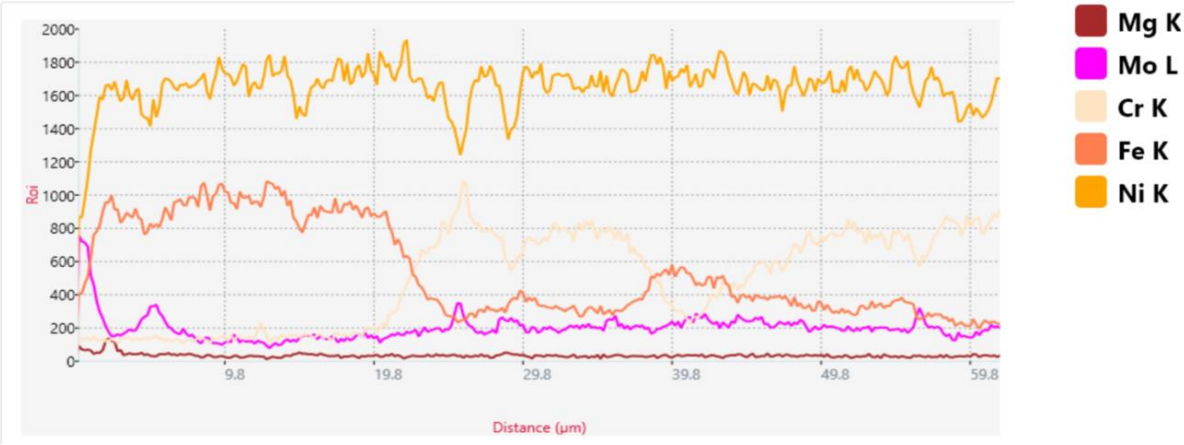

Figure 42: Element Profile of Cross Section EDS Line Scan of Cut Inconel 625 Area 1

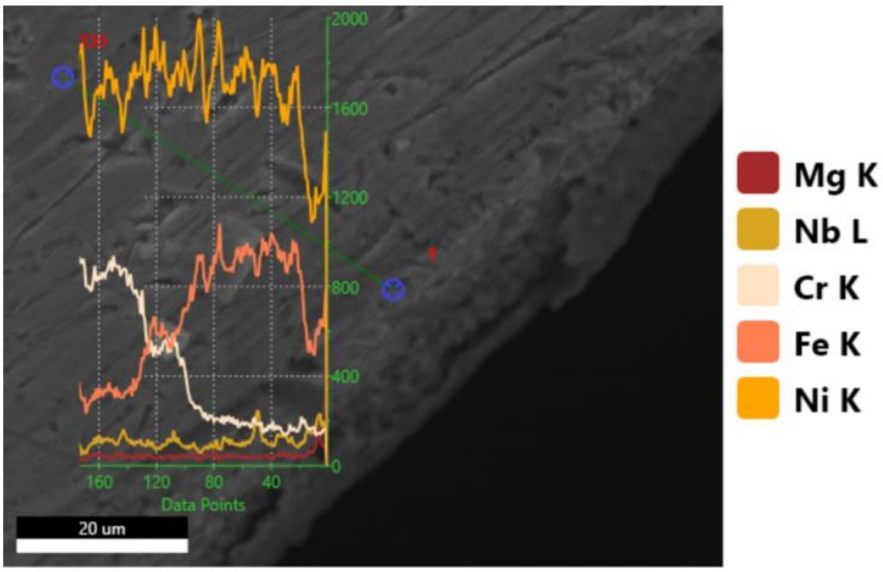

Figure 43: Cross Section EDS Line Scan of Cut Inconel 625 Area 2

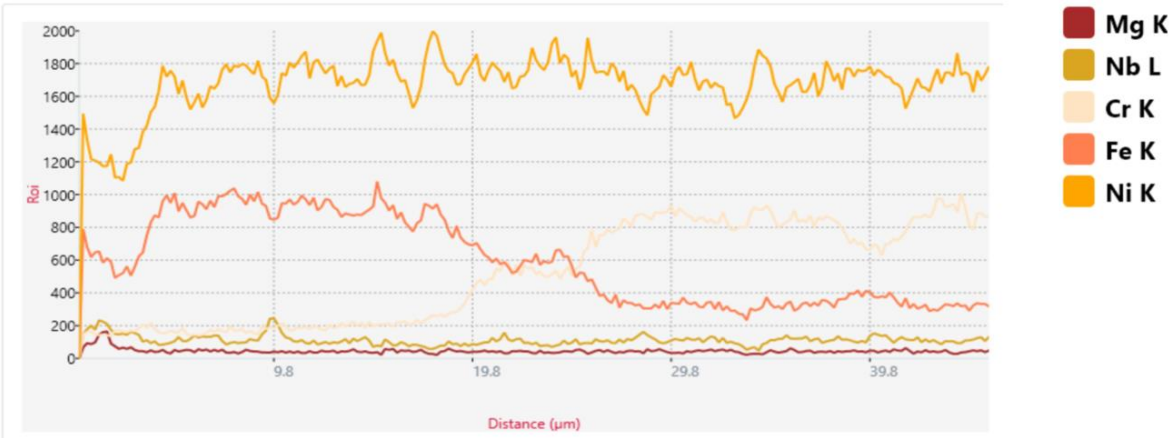

Figure 44: Element Profile of Cross Section EDS Line Scan of Cut Inconel 625 Area 2

Figures 45-48 show the results of EDS line scan analysis on the cut face of Inconel 740H samples. Visually, significant pitting corrosion and corrosion damage was visible in the first 5-10 μm from sample exterior. Proceeding deeper into the samples, some pitting corrosion was visible, but ultimately very little in comparison to the density of pitting at the edge. EDS line scan analysis appears noisy on Inconel 740H as a high number of data points was needed. Pockets of un-depleted chromium and other unexpected inconsistencies made scans with lower data points challenging to interpret. One such instance can be seen in the chromium spike and decrease in cobalt, nickel, and iron 10-20 μm from the edge in Figure 45, likely the result of a pocket of un-depleted chromium. Using a high data point count, the line scan showed clear chromium depletion in Inconel 740H until approximately 35-40 μm depth. In the same range, iron content increased, possibly replacing the chromium or also being pulled out from the alloy by the chloride salt. Nickel content held mostly constant throughout the length of the line scan on the cut surface, however it also responded to inconsistencies near the edge such as chromium spikes.

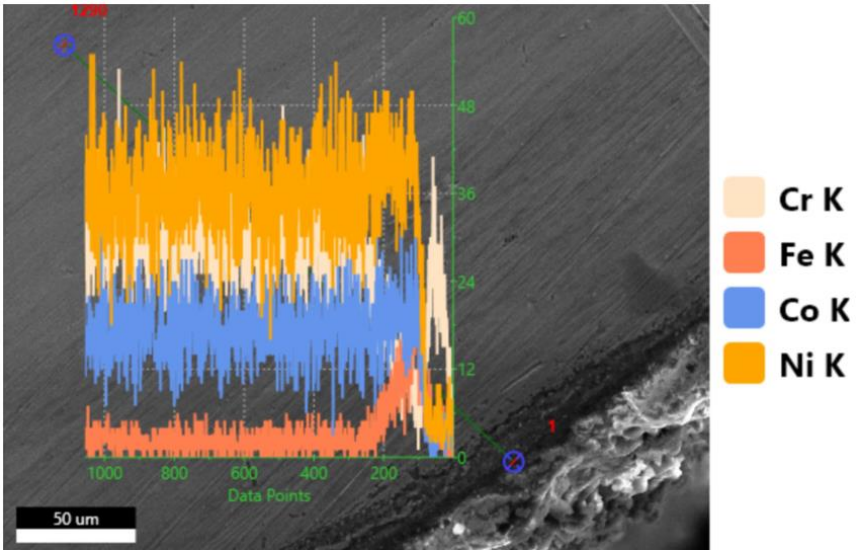

Figure 45: Cross Section EDS Line Scan of Cut Inconel 740H Area 1

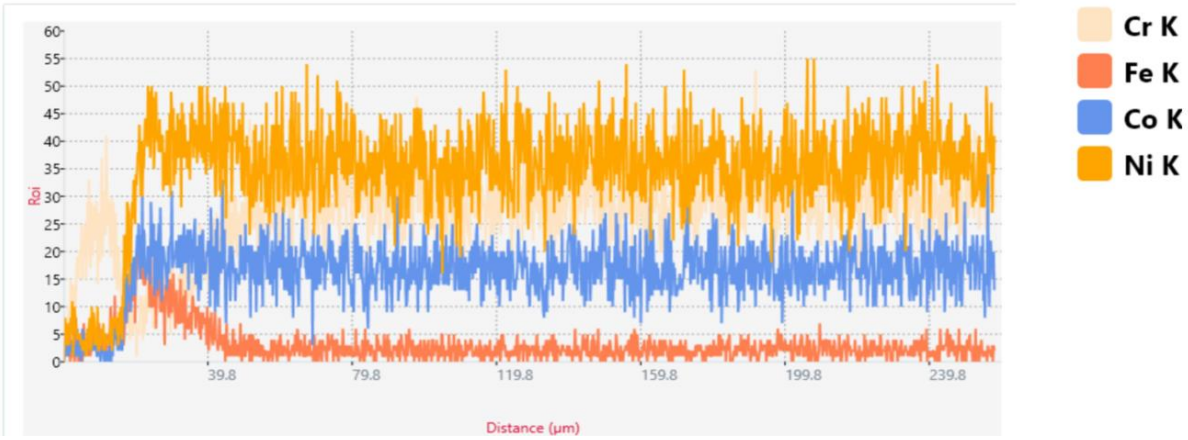

Figure 46: Element Map of Cross Section EDS Line Scan of Cut Inconel 740H Area 1

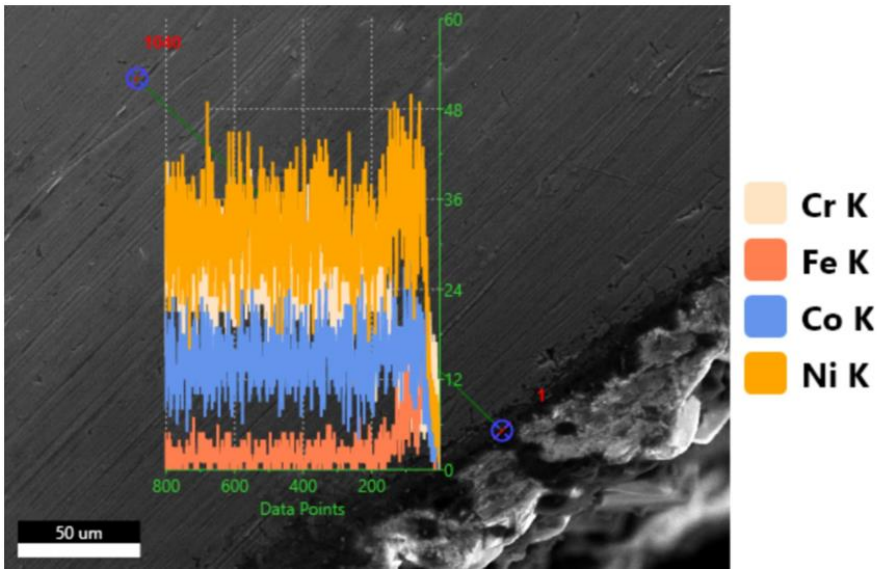

Figure 47: Cross Section EDS Line Scan of Cut Inconel 740H Area 2

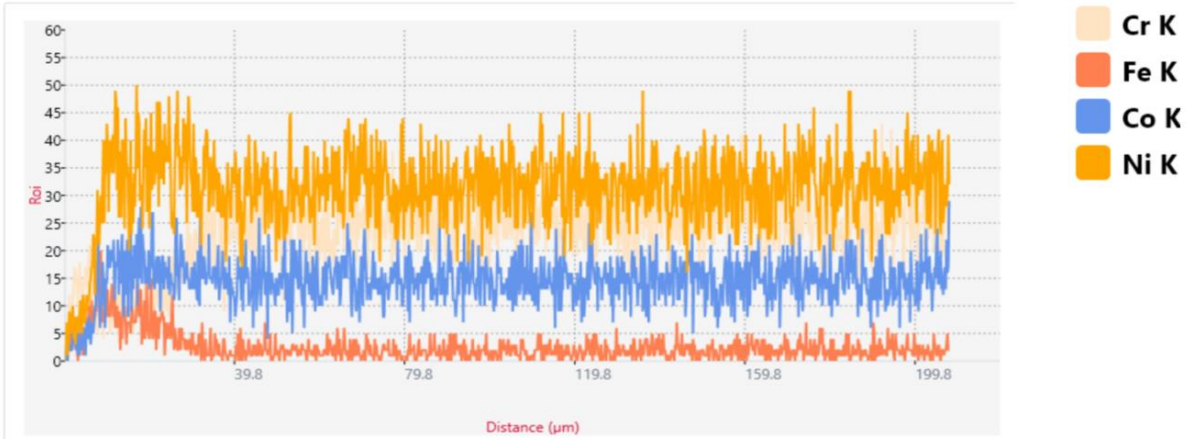

Figure 48: Element Map of Cross Section EDS Line Scan of Cut Inconel 740H Area 2

Finally, Hayne 282 samples were imaged last, with Figures 49-52 showing the EDS line scans and element maps. Some damage and possible signs of corrosion could be seen near the edge of the sample. The damage was not as obviously due to corrosion as the pitting seen on previous materials, it is possible the damage was due to cutting and polishing. The cut faces of the Haynes 282 samples were overall in much worse condition than the other materials, with many deformities and significant damage near the edges. However, EDS elemental composition did show clear signs of corrosion. Chromium depletion with elevated iron and cobalt levels was visible in the first ~40 μm of the samples. The decline of chromium content was notably sharp rather than gradual. Though the surfaces were heavily damaged, the chromium depletion did seem to correspond with darkening and damage near the edges. These results indicate Haynes 282 chloride salt corrosion at least to the 40 μm depth. Nickel content held constant throughout the length of the line scans on the cut surface.

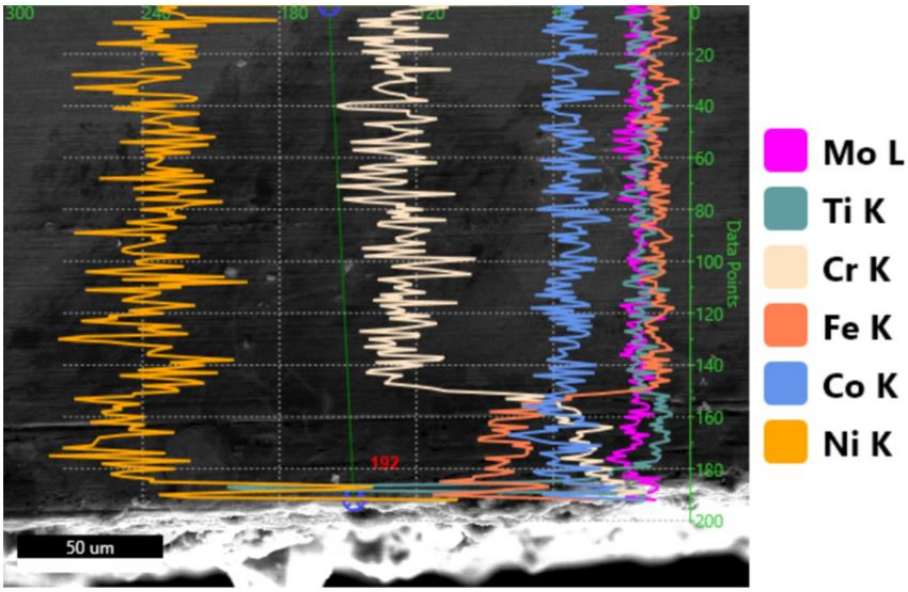

Figure 49: Cross Section EDS Line Scan of Haynes 282 Cut Face Area 1

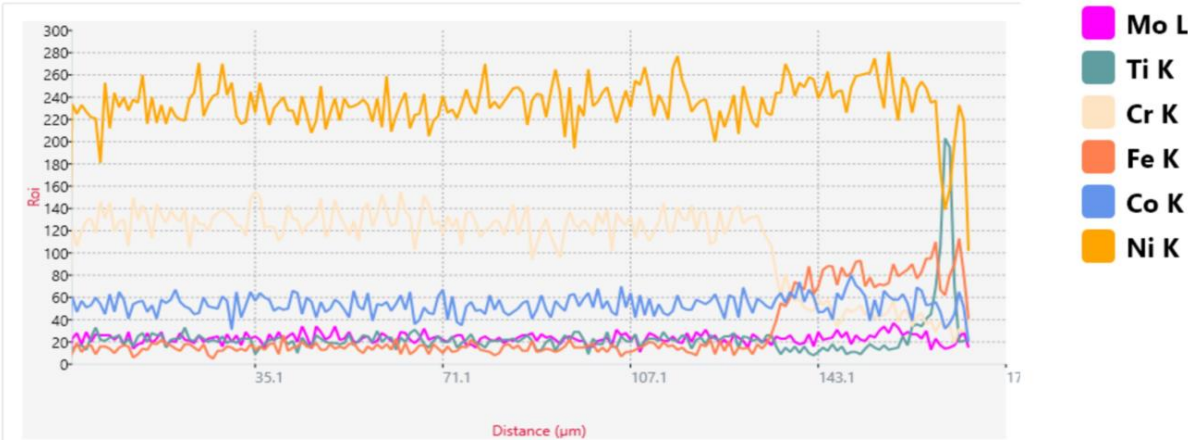

Figure 50: Element Map for Cross Section EDS Line Scan of Haynes 282 Cut Face Area 1

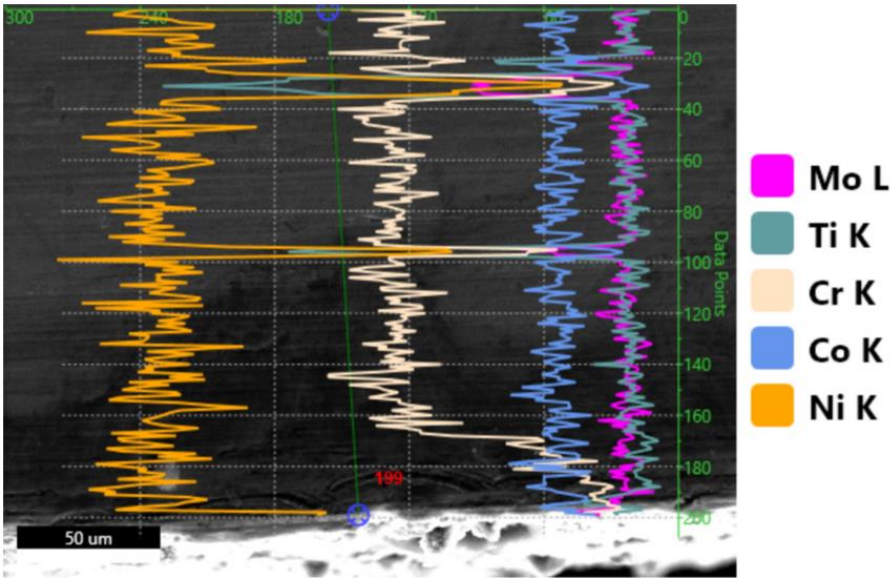

Figure 51: Cross Section EDS Line Scan of Haynes 282 Cut Face Area 2

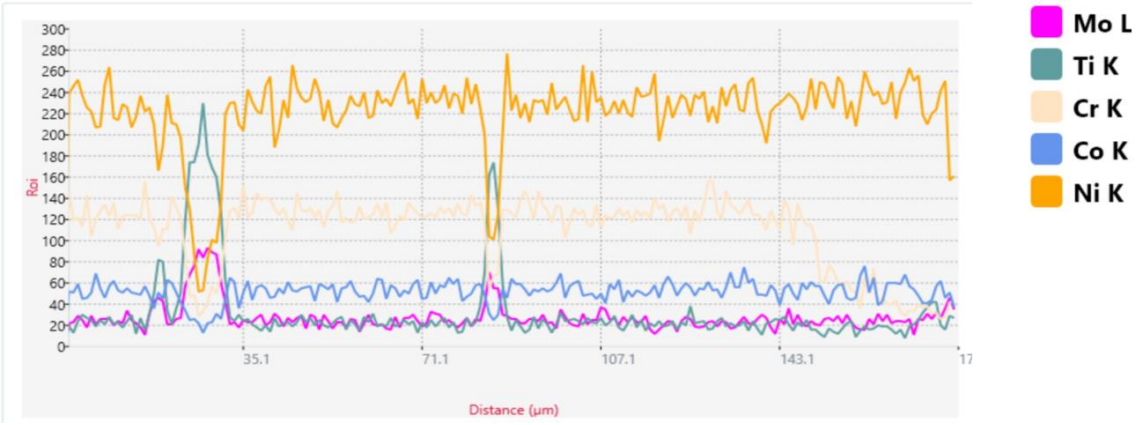

Figure 52: Element Map for Cross Section EDS Line Scan of Haynes 282 Cut Face Area 2

In addition to the line scans previously shown for Haynes 282, additional scans were taken to evaluate aluminum content. After the findings of the exterior surface EDS element mapping, which showed high aluminum content, the line scans shown in Figures 53 and 54 were taken to evaluate potential aluminum depletion. Across the length of the line scan on the cut face, aluminum content was consistently low. The line scan was extended to terminate on the exterior surface of the sample, where aluminum content spiked.

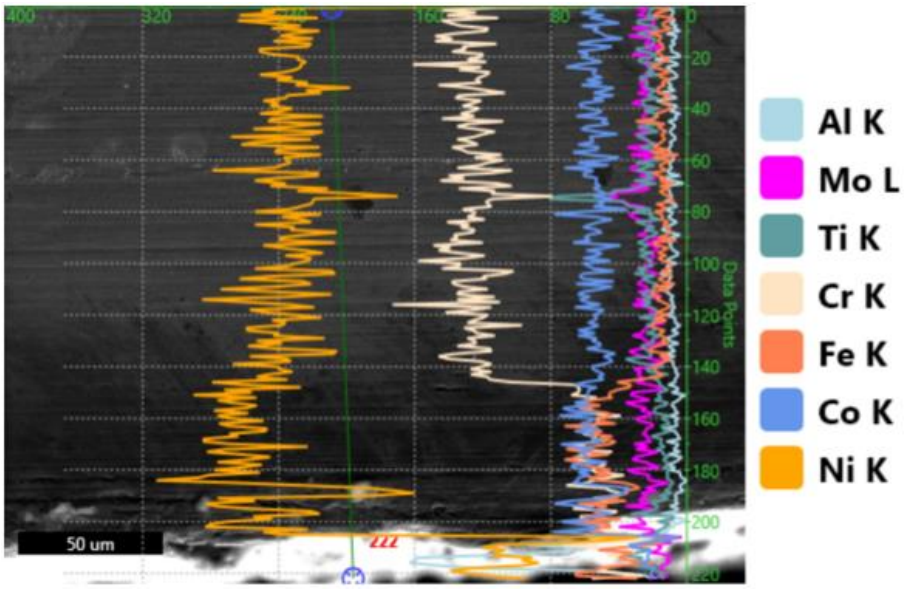

Figure 53: Cross Section EDS Line Scan of Haynes 282 Cut Face Area 3

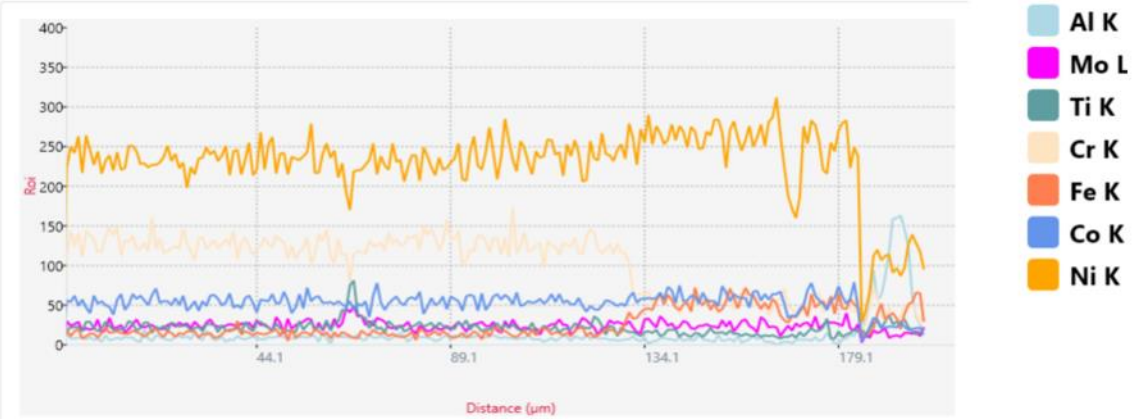

Figure 54: Element Map for Cross Section EDS Line Scan of Haynes 282 Cut Face Area 3

Though only two scans were shown for each material type, many scans were taken on all the multiple samples of each material type. The depth of chromium depletion and corrosion indicators seen in each of these scans, for each sample, was averaged to determine the depth of corrosion for the material in the presence of 750 °C ternary chloride salt. Table 10 provides these statistics for depths of chromium depletion and corrosion indicators.

Table 10: Chromium Depletion of Nickel Alloys

Alloy Type	Maximum Depth of Chromium Depletion and Corrosion Indicators (µm)	Minimum Depth of Chromium Depletion and Corrosion Indicators (µm)	Average Depth of Chromium Depletion and Corrosion Indicators (µm)
Inconel 625	55	20	32.13
Haynes 230	40	33	36.25
Haynes 282	55	30	41.00
Inconel 740H	53	39	47.67
Inconel 800H	310	70	247.37

3.3.3 Salt XRD Analysis

In addition to SEM and EDS analysis, a Chemical Engineer at SNL performed X-Ray Diffraction (XRD) analysis on the salt after chloride salt after the 500-hour corrosion study was performed. Figures 55-57 show the XRD analysis of the salt used in this test. It appears the carnallite is the primary component, with sodium chloride mixed in. The individual KCl and $MgCl_2$ phases did not show up in the analysis, possibly suggesting there was a phase change during the test. Carnallite can be synthesized by mixing KCl and $MgCl_2$, potentially contributing to the change in composition post-test. Notably, no nickel, nickel oxide, or other dissolved alloying elements could be identified. One peak could not be identified to satisfaction, however as it was not in line with any salt components or common alloying elements it could be a contamination in this sample or a minor alloying element from one of the alloys.

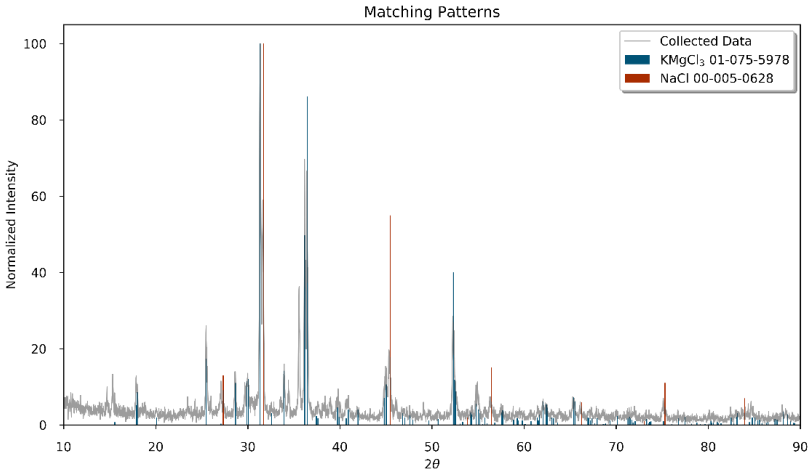

Figure 55: XRD analysis of post-test salt

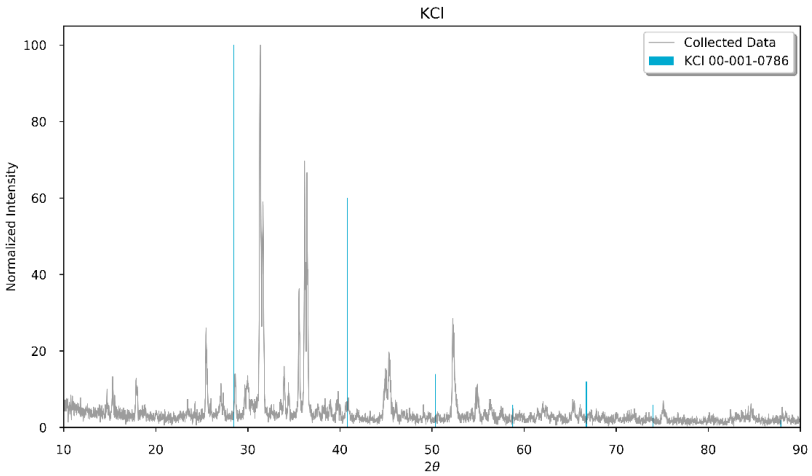

Figure 56: XRD analysis of post-test salt

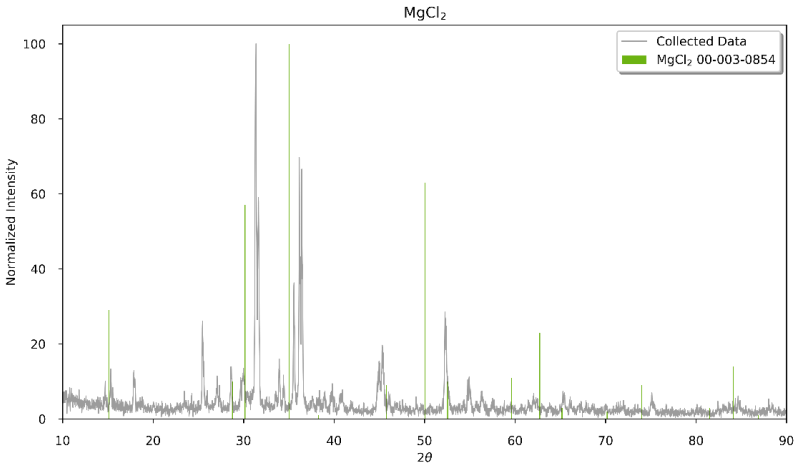

Figure 57: XRD analysis of post-test salt

CHAPTER FOUR: DISCUSSION

For the five nickel alloys reviewed in this work, there are many metrics to evaluate corrosion resistance and chloride salt compatibility. Data collected includes visual observations, mass change of samples, calculated corrosion in μm/year, calculated corrosion in mg/cm^2, SEM and EDS element mapping of sample surfaces, and SEM and EDS element line scanning of cut and polished sample faces. All quantitative data is summarized in Table 11 below. All results are averaged from the data obtained for each of the three samples per alloy.

Table 11: Summary of Quantitative Data Describing Alloy Behavior in 750 °C Ternary Chloride Salt for 500 Hours

Alloy Type	Average Mass Change (grams)	Average Percent Mass Change (%)	Corrosion Rate (μm/year)	Corrosion Rate (mg/cm^2)	Average Depth of Chromium Depletion (μm)
Inconel 625	-0.0465	-0.1306	-48.4364	-2.4042	32.1300
Haynes 230	-0.0087	-0.0479	-10.6586	-0.5394	36.2500
Haynes 282	-0.0427	-0.3144	-69.9625	-3.3742	41.0000
Inconel 740H	+0.1717	+0.4759	+176.4999	+8.8729	47.6700
Inconel 800H	-0.8829	-2.5329	-939.3167	-45.6166	247.3700

Of the five alloys analyzed in this work, Inconel 800H was the worst performer. After 500 hours in the test pot with ternary chloride salt at 750 °C, the sample was visibly damaged. To the naked eye without magnification tools, the pitting corrosion of the Inconel 800H samples was clearly visible. The three Inconel 800H samples had extreme mass change in the salt, averaging almost a gram lost in 500 hours. The samples lost an average of 2.53% mass/500 hours, 8 times higher than the next highest average mass loss and 53 times higher than the lowest average mass loss. Even more staggering is this corrosion rate of the material. Based on the mass loss, material density, and sample surface area, Inconel 800H showed calculated corrosion rates of -939.32 μm/year and -45.62 mg/cm^2. This corrosion rate is significant, far beyond what is acceptable for use in high temperature flow loops of any kind. Confirmation of the extreme

calculated corrosion rates came from SEM and EDS analysis. At the surface level, Inconel 800H had high indicators of corrosion and chromium depletion. Interior line scans of cut and polished samples indicated that the Inconel 800H experienced an average corrosion depth of 247.37 μm. The lowest depth of chromium depletion that could be found after extensive analysis was 70 μm, still considerably deep, while the highest was 310 μm. This corrosion is catastrophic, and in a full-scale ternary chloride salt flow loop it could lead to failure of components constructed of Inconel 800H after little time. If the corrosion rate of almost 1 mm/year held constant, ternary chloride salt could reduce Inconel 800H pipe wall by $1/16^{th}$ of an inch in just 1.6 years. With this short of a service lifetime, Inconel 800H could be considered unusable.

Inconel 740H is the outlier in this test, as the only material that gained mass. The finding does not appear to be flawed, all three Inconel 740H samples exhibited the same behavior. Not one sample lost mass, and the average mass gain for the material was 0.17 grams. This is a percent mass gain of 0.48%, a significant amount for a 500-hour exposure time. Based on the mass gain, material density, and sample surface area, Inconel 740H showed calculated material change rates of +176.50 μm/year and +8.87 mg/cm^2. A gain in mass can be just as catastrophic as corrosion, reducing the diameter of piping and creating particulate that could break off and damage downstream components. SEM and EDS analysis offers further insight into the phenomenon. EDS line scans on sample cut and polished faces reveal that, though the material ultimately gained weight, the samples were corroded. An average depth of 47.67 μm chromium depletion was observed. SEM and EDS element mapping on the sample exterior surfaces revealed large deposits of salt residue covering the exterior faces. This residue could not be removed even after sonicating in a deionized water bath. This salt residue was a mix of amorphous salt and depleted alloying elements, particularly chromium, nickel, and iron.

Considering all of this information, it can be inferred that the Inconel 740H samples were in fact corroded. After the alloying elements were depleted, however, some of these elements reprecipitated on the surface of the samples. The salt residue is found because the elements were either dissolved in the salt or the reprecipitated elements created a rough surface within which the salt became trapped. This resulted in the consistent mass gain.

The Haynes 282 samples performed reasonably well. All three samples lost mass after 500 hours in the 750 °C ternary chloride salt. The average mass loss was 0.042 grams, an average percent loss of 0.31%. Visually, the sample did have some signs of corrosion and salt deposits on the surface that remained after washing, though not nearly as significant as those found on the Inconel 740H samples. However, the samples overall salt compatibility is not ideal. Haynes 282 exhibited calculated material change rates of -70.00 μm/year and -3.37 mg/cm^2. An average depth of 41.00 μm chromium depletion was observed via EDS line scans of the sample body interiors. SEM and EDS imaging of the sample exterior surfaces revealed that in addition to the chromium depletion, there may have also been significant aluminum depletion. A layer of aluminum was determined to be covering much of the exterior surface of the samples, a layer which also seemed to correspond with deposits of salt. A line scan of a samples cross sectional cut and polished face showed that the aluminum content remained at a constant, low level at least 220 μm deep into the sample before spiking to much higher concentrations at the exterior. It is possible that the aluminum was depleted out of the Haynes 282 along with the chromium, and reprecipitated on the sample exterior surface in salt residue deposits in a mechanism similar to that seen on the Inconel 740H samples. This finding makes the actual corrosion difficult to determine, as it is possible the sample was more seriously corroded than this data suggests. The

mass loss would be offset by the mass gain resulting from the deposits on the exterior surfaces, making the mass loss and corrosion rates appear lower and not representative of the true damage the samples endured.

The best performing samples in this study were those of Inconel 625 and Haynes 230. The Haynes 230 samples had the overall lowest mass loss and corrosion rates. With an average mass loss of 0.009 grams, the Haynes 230 samples only lost an average 0.05% mass. Based on the mass loss, material density, and sample surface area, Haynes 230 showed calculated corrosion rates of -10.66 μm/year and -0.54 mg/cm^2. These corrosion rates are significantly low for any material in ternary chloride salt at high temperatures. The SEM and EDS analysis showed little signs of corrosion on the exterior surfaces of the samples. One area analyzed did show significant coverage with salt deposits, however the salt did not contain reprecipitated alloying elements like other materials in this test. The deposits were almost pure magnesium oxide, and they did not cover the entire sample. Many surface images were taken where no salt deposits were detected. The EDS line scans of the cut and polished faces revealed little visible pitting corrosion and chromium depletion at an average of 36.25 μm deep.

Inconel 625 corrosion metrics were also low, outperforming Haynes 230 in some areas. Inconel 625 samples lost an average of 0.05 grams, corresponding to an average percent mass loss of 0.13%. Based on these losses, the Inconel 625 samples showed average calculated corrosion rates of -48.44 μm/year and -2.40 mg/cm^2. While these values were not as low as Haynes 230, Inconel 625 showed little signs of corrosive damage in SEM and EDS analysis. The surface imaging of Inconel 625 samples showed almost no signs of corrosion, with high levels of nickel, iron, and chromium remaining at the exterior surfaces and no visible damage or

significant salt deposits. Upon scanning the interior via line scans of cut and polished faces, an average chromium depletion up to 32.13 µm deep was observed. In addition, the lowest chromium depletion rate found in Inconel 625 sample scanning was only 20 µm deep, the lowest depletion depth found in this study. Almost no pitting corrosion or damage was visible during analysis of the cut faces.

Overall, a broad range of alloy compatibility was observed between the five alloys experimentally exposed to molten chloride salt in this work. Some alloys stood out as excellent candidates for use in high temperature ternary chloride salt systems, while others stood out for extreme corrosion rates which would cause rapid failure of a full-scale system.

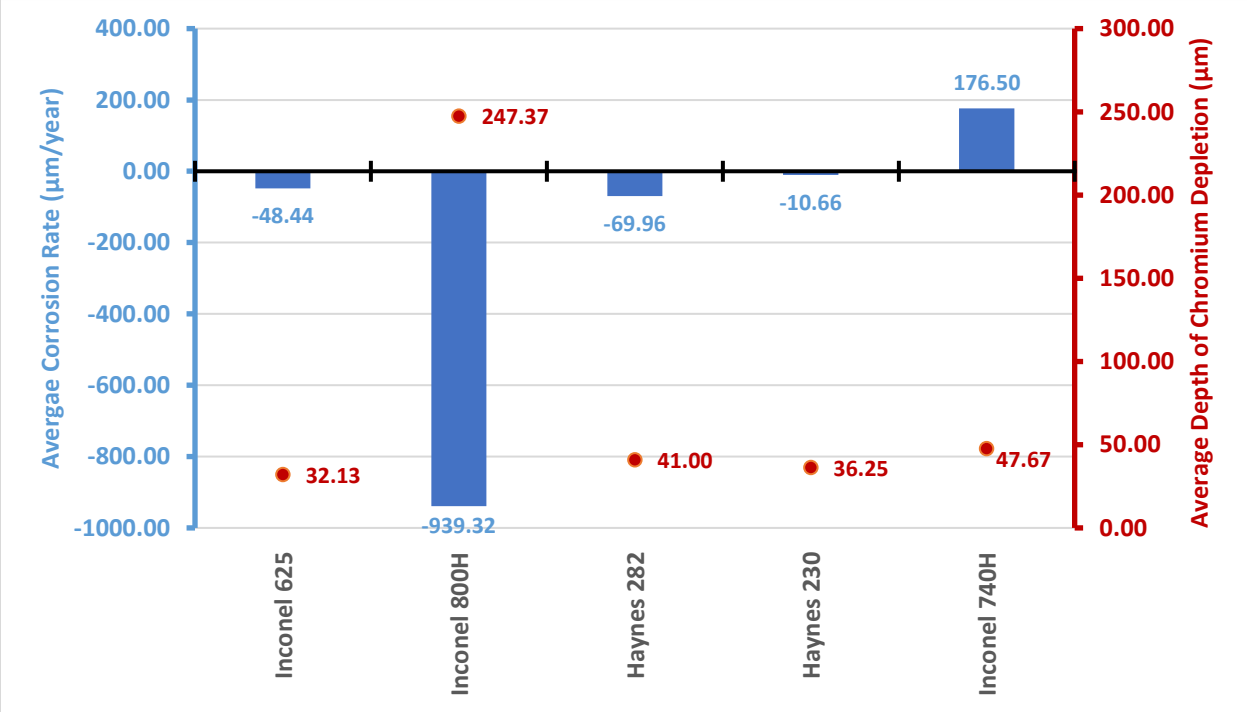

Figure 58: Corrosion Rate and Average Depth of Chromium Depletion, by Alloy

Haynes 230 and Inconel 625 were the best performing alloys tested in this work. Inconel 625 showed the lowest observed and lowest average chromium depletion, with almost no signs of significant corrosion or damage found in SEM and EDS analysis. Haynes 230 also had low

chromium depletion and had the lowest mass loss and corrosion rates of all five materials tested. Comparing the SEM and EDS data between these materials is challenging, as the Inconel 625 samples ultimately had more line scan data and a wider range of chromium depletion values to analyze. Inconel 625 samples had chromium depletions observed at depths between 20-55 μm, across many line scans on each sample. Fewer line scans exist for the Haynes 230 samples, across a tighter range of 33-40 μm. Considering that Haynes 230 did show the lowest average corrosion rate, four times lower than that of Inconel 625, while also showing an appreciably low depth of corrosion, Haynes 230 could be considered the best alloy candidate tested. Inconel 740H, Haynes 282, and Inconel 800H all showed problematic compatibility with the ternary chloride salt. The differences in compatibility with the salt between the five alloys can be attributed to the elemental compositions. As previously mentioned in Chapter One, chloride salt corrosion mechanism can be directly correlated with chromium content [23],[24]. All five alloys in this test have similar chromium content. However, while Haynes 230 and Inconel 625 have high nickel and low iron content, Inconel 800H has the lowest nickel content and highest iron content of all alloys tested. Inconel 800H is between 88.5-97.5% nickel, iron, and chromium, with the remainder composed of just aluminum, titanium, and carbon. Considering chloride salt corrosion mechanisms and specific alloying element depletion, Inconel 800H corrosion rates are expected. The lack of refractory elements in Inconel 800H could be equally detrimental to its performance, as the inclusion of refractory elements cobalt, molybdenum, and tungsten have been shown to improve chloride salt corrosion resistance [32]. Haynes 230 and Inconel 625 both likely performed so well because these metals have the highest nickel content, low iron content, and refractory metal content. Inconel 625 has high molybdenum and a small percent cobalt, while Haynes 230 has high cobalt and some molybdenum. Importantly, Haynes 230 also has

14% tungsten. No other alloys in this test had tungsten content. This could be why Haynes 230 arguably had the best performance. Yet Inconel 740H and Haynes 282 also have high nickel, cobalt, molybdenum, and low iron, yet neither performed as well as Haynes 230 and Inconel 625. For Inconel 740H, this could be due to the fact that nickel content is allowed to be as low as 38%. It could also be due to the inclusion of copper, an element that does not appear in any of the other alloys. Haynes 282 is more enigmatic, as it has the lowest iron content of all the alloys, nickel content as high as Haynes 230, molybdenum content as high as Inconel 625, and cobalt content higher than either. One explanation is that cobalt simply isn't as useful of a refractory element to include, as both Haynes 282 and Inconel 740H have notably high cobalt but performed poorly while Inconel 625 and Haynes 230 have much lower cobalt. Another unique observation with Haynes 282 was the possible depletion of aluminum. Haynes 282 appeared to exhibit aluminum depletion and reprecipitation on the sample surfaces. Haynes 282 also had aluminum content almost four times higher than the next highest alloy.

In comparison to the data found as part of the previous literature review in Chapter One, these corrosion results were mostly expected, as show in Table 12. Direct comparison cannot easily be made as some of the data collected in literature comes from tests with different chloride salts like, and in test conditions that differ from those used in our test. In addition, for some alloys such as Inconel 740H Haynes 282, no data could be found in literature. For this reason, only a reduced number of values from literature are included here as opposed to Table 3 where a full literature review can be found. In Table 12, the values included are from tests with similar temperatures and test durations to our 750 °C, 500-hour test conditions at SNL.

Table 12: Comparison of Corrosion Data to Results in Literature

Alloy Type	Literature	Literature	Literature	SNL	SNL	SNL

	Mass loss/gain (mg/cm^2)	Corrosion Rate (μm/year)	Corrosion Depth (μm)	Observed Mass loss/gain (mg/cm^2)	Observed Corrosion Rate (μm/year)	Observed Average Corrosion Depth (μm)
Inconel 625	-1.6 [47]	-33.71 [47]	26 [47]	-2.40	-48.44	32.13
Haynes 230	-0.55 [49]	-27 [15]	31.6 [15]	-0.54	-10.66	36.25
Haynes 282				-3.37	-69.96	41.00
Inconel 740H				+8.87	+176.50	47.67
Inconel 800H	-13.1 [50]	-364 [51]	50 [51]	-45.62	-939.32	247.37

Inconel 625 values from literature were lower than those observed in this test, however the low values come from a paper where $MgCl_2$ salt was used for the corrosion study. This data was still included for comparison because it is the only chloride salt corrosion reference for Inconel 625 that could be found. Haynes 230 values from literature have a wide spread of data across many salt variations, temperatures, test conditions, and end results. The data in Table 12 comes from two specific tests with test conditions similar to those at SNL, where one study in the same NaCl-$MgCl_2$-KCl salt found almost identical corrosion in units of mg/cm^2. Similar values to SNL observations were also reported in literature for corrosion depth by chromium depletion. Greater corrosion in μm/year was reported for Haynes 230, though the value was still relatively low. Inconel 800H values in literature were not as high as those observed at SNL, however the trend is similar. Corrosion values for Inconel 800H in the body of published chloride salt corrosion studies are amongst the very highest. For the remaining two alloys Haynes 282 and Inconel 740H, data could not be found.

CHAPTER FIVE: CONCLUSION

At the beginning of this work it was determined through literature review that, for the future of next generation CSP projects, more useful engineering data was needed. While existing data is useful from a scientific standpoint, inconsistencies between test conditions, salt types, test durations, and test temperatures make it challenging to compare data points to make informed engineering design decisions. Engineers require data from consistent methodology, with identical temperature, duration, salt type, and test conditions, for a broad selection of materials. With this information, comparison of material corrosion and behavior in molten salt could more easily be made in order to make the best designs for next generation CSP. To answer this demand for data, a corrosion test series was started at the National Solar Thermal Test Facility of Sandia National Laboratories. A multi-chamber test system was designed and constructed to allow for dozens of material test samples to be submerged in purified ternary chloride salt (20% NaCl/40% $MgCl_2$/40% KCl by mol wt %) at 750 °C, for durations of 500 hours. Though hundreds of samples from dozens of material types have been put through this test system, five high nickel alloys of particular academic and industry interest have been assessed in this paper. Some alloys performed well, while some proved not at all acceptable for possible engineering and development of chloride salt system components. Considering the data presented in Table 11, two alloys stand out as legitimate candidates for use in high temperature ternary chloride salt flow loop components: Inconel 625 and Haynes 230. Inconel 625 was visibly the least corroded sample and had the lowest single measurement and overall average chromium depletion. Haynes 230 had respectably low chromium depletion, along with the lowest mass loss and calculated corrosion rates. Haynes 282 showed issues with chromium depletion significantly higher than Inconel 625 and Haynes 230. Haynes 282 data also presented evidence of potentially problematic

aluminum depletion, leading to further sample damage and development of aluminum-salt residue deposits on the exterior sample surfaces. Inconel 740H had high chromium depletion and significant mass gain due to reprecipitation of alloying elements in a residue mixture on the exterior surfaces. The high corrosion rates of Inconel 740H and Haynes 282, combined with the concerning reprecipitation of depleted alloying elements on the sample surfaces, could be problematic for design of a full-scale ternary chloride salt flow loop. Salt deposits and reprecipitated alloys could alter component diameters or break off and damage downstream components. Inconel 800H showed extremely high corrosion and mass loss, so high that a full-scale loop could be permanently damaged within mere months of operation if corrosion rates held steady. At almost -1 mm/year corrosion, Inconel 800H likely should not be in contact with ternary chloride salt. Ultimately, either Inconel 625 or Haynes 230 could make good candidates for ternary chloride salt flow loop construction at design temperatures of 750 °C. Both showed significant promise as construction materials and far outperformed the other alloy candidates. Yet outside the implications for individual alloy usability, the true importance of this work lies in the complete collection of data for all five alloys considered as a whole. For alloys like Inconel 625, this study represents one of the only chloride salt corrosion studies and the first data set that could be found for corrosion in this ternary salt chemistry. For Inconel 740H and Haynes 282, this study represents the only chloride salt corrosion data that could be found. By creating a standardized environment with the same temperature, atmosphere, test duration, salt chemistry, and salt purity, these five alloys and the many others tested can all be compared against one another. We hope that with this presented and growing body of data from standardized testing, engineers will be able to better evaluate and design next generation, high temperature heat storage and heat transfer systems for industries such as CSP.

REFERENCES

[1] M.S. Al-Soud, E.S. Hrayshat, A 50MW concentrating solar power plant for Jordan, Journal of Cleaner Production, 17 (2009) 625-635.

[2] Z. Wang, Z. Yao, J. Dong, J. Hongguang, W. Han, Z. Lu, X. Wei, The Design of a 1MW Solar Thermal Tower Plant in Beijing, China, in: International Solar Energy Society World Congress, Springer Berlin, Heidelberg, 2007, pp. 1729–1732.

[3] A. Boretti, Concentrated Solar Power Plants Capacity Factors: A Review, in: Nonlinear Approaches in Engineering Applications, 2018, pp. 41-62.

[4] K. Madaly, Identifying the optimum storage capacity for a 100-MWe concentrating solar power plant in South Africa, in: Faculty of Engineering, Stellenbosch University, 2014.

[5] G. Mohan, M. Venkataraman, J. Gomez-Vidal, J. Coventry, Assessment of a novel ternary eutectic chloride salt for next generation high-temperature sensible heat storage, Energy Conversion and Management, 167 (2018) 156-164.

[6] G. Mohan, M.B. Venkataraman, J. Coventry, Sensible energy storage options for concentrating solar power plants operating above 600 °C, Renewable and Sustainable Energy Reviews, 107 (2019) 319-337.

[7] K.M. Armijo, M.D. Carlson, D. Dorsey, J.M. Christian, J. Coventry, R. McNaughton, C. Turchi, Design Basis for a 2.0MWth Liquid-HTF Pilot-Scale CSP System, in: Asia-Pacific Solar Research Conference, Canberra, Australia 2019.

[8] M. Mehos, C. Turchi, J. Jorgenson, P. Denholm, C. Ho, K. Armijo, On the Path to SunShot - Advancing Concentrating Solar Power Technology, Performance, and Dispatchability, in, National Renewable Energy Laboratory, 2016.

[9] K.M. Armijo, S.L. Shinde, Heat Transfer Phenomena in Concentrating Solar Power Systems, in, Sandia National Laboratories, 2016.

[10] M. McPherson, M. Mehos, P. Denholm, Leveraging concentrating solar power plant dispatchability: A review of the impacts of global market structures and policy, Energy Policy, 139 (2020).

[11] M. Paskevicius, D.A. Sheppard, K. Williamson, C.E. Buckley, Metal hydride thermal heat storage prototype for concentrating solar thermal power, Energy, 88 (2015) 469-477.

[12] P. Gimenez, S. Fereres, Effect of Heating Rates and Composition on the Thermal Decomposition of Nitrate Based Molten Salts, Energy Procedia, 69 (2015) 654-662.

[13] H. Benoit, L. Spreafico, D. Gauthier, G. Flamant, Review of heat transfer fluids in tube-receivers used in concentrating solar thermal systems: Properties and heat transfer coefficients, Renewable and Sustainable Energy Reviews, 55 (2016) 298-315.

[14] C.S. Turchi, J. Vidal, M. Bauer, Molten salt power towers operating at 600–650 °C: Salt selection and cost benefits, Solar Energy, 164 (2018) 38-46.

[15] Y. Zhao, Molten Chloride Thermophysical Properties, Chemical Optimization, and Purification, in, National Renewable Energy Laboratory, 2020.

[16] J. Vidal, N. Klammer, Molten chloride technology pathway to meet the U.S. DOE sunshot initiative with Gen3 CSP, in: SOLARPACES 2018: International Conference on Concentrating Solar Power and Chemical Energy Systems, AIP Publishing, Casablanca, Morocco, 2018.

[17] N. Klammer, C. Engtrakul, Y. Zhao, Y. Wu, J. Vidal, Method To Determine MgO and MgOHCl in Chloride Molten Salts, Analytical Chemistry, 92 (2020) 3598-3604.

[18] W. Ding, A. Bonk, T. Bauer, Molten chloride salts for next generation CSP plants: Selection of promising chloride salts & study on corrosion of alloys in molten chloride salts, in: SOLARPACES 2018: International Conference on Concentrating Solar Power and Chemical Energy Systems, Casablanca, Morocco, 2019.

[19] G. Mohan, M. Venkataraman, J. Gomez-Vidal, J. Coventry, Thermo-economic analysis of high-temperature sensible thermal storage with different ternary eutectic alkali and alkaline earth metal chlorides, Solar Energy, 176 (2018) 350-357.

[20] A. Veluchamy, D. Sherwood, B. Emmanuel, I.S. Cole, Critical review on the passive film formation and breakdown on iron electrode and the models for the mechanisms underlying passivity, Journal of Electroanalytical Chemistry, 785 (2017) 196-215.

[21] Y. Song, G. Jiang, Y. Chen, P. Zhao, Y. Tian, Effects of chloride ions on corrosion of ductile iron and carbon steel in soil environments, Sci Rep, 7 (2017) 6865.

[22] A. Kruizenga, Corrosion mechanisms in chloride and carbonate salts, in, andia National Laboratories, 2012.

[23] Y.S. Li, M. Spiegel, S. Shimada, Corrosion behaviour of various model alloys with NaCl–KCl coating, Materials Chemistry and Physics, 93 (2005) 217-223.

[24] S. Vuelvas-Rayo, J.G. Gonzalez-Rodriguez, J. Porcayo-Calderon, V.M. Salinas-Bravo, S.I. Maldonado-Ruiz, Hot Corrosion Behavior of High-Chromium, High-Carbon Cast Irons in NaCl-KCl Molten Salts, International Journal of Corrosion, 2012 (2012) 1-9.

[25] S. Lim, Y. Kang, H. Lee, S. Shin, Design optimization of a tubular solar receiver with a porous medium, Applied Thermal Engineering, 62 (2014) 566-572.

[26] M. Marko, Molten nitrate salt solar central receiver of low cycle fatigue 625 alloy, in, Solarreserve Technology LLC United States, 1996.

[27] T. Bauer, N. Pfleger, N. Breidenbach, M. Eck, D. Laing, S. Kaesche, Material aspects of Solar Salt for sensible heat storage, Applied Energy, 111 (2013) 1114-1119.

[28] R.I. Dunn, P.J. Hearps, M.N. Wright, Molten-Salt Power Towers: Newly Commercial Concentrating Solar Storage, Proceedings of the IEEE, 100 (2012) 504-515.

[29] S. Freund, M. Abarr, J.D. McTigue, K.L. Frick, A. Mathur, D. Reindl, A.V. Asselt, G. Casubolo, Thermal energy storage, in: Thermal, Mechanical, and Hybrid Chemical Energy Storage Systems, Academic Press, 2021, pp. 65-137.

[30] M. Liu, N.H. Steven Tay, S. Bell, M. Belusko, R. Jacob, G. Will, W. Saman, F. Bruno, Review on concentrating solar power plants and new developments in high temperature thermal energy storage technologies, Renewable and Sustainable Energy Reviews, 53 (2016) 1411-1432.

[31] H.S. Klapper, N.S. Zadorozne, R.B. Rebak, Localized Corrosion Characteristics of Nickel Alloys: A Review, Acta Metallurgica Sinica (English Letters), 30 (2017) 296-305.

[32] I.V. Oryshich, O.S. Kostyrko, Infleuence of molybdenum, tungsten, and cobalt on the corrosion of high-temperature strength nickel alloys in molten salts, Metal Science and Heat Treatment, 27 (1985) 740-746.

[33] HAYNES® 230® Alloy Data Sheet, in, Haynes International, 2021.

[34] Special Metals Inconel 617 Technical Bulletin, in, Special Metals Corporation, 2005.

[35] HASTELLOY® C-276 Alloy Data Sheet, in, Haynes International, 2020.

[36] Special Metals Inconel 625 Technical Bulletin, in, Special Metals Corporation, 2013.

[37] Special Metals Inconel 740H Technical Bulletin, in, Special Metals Corporation, 2015.

[38] Special Metals Incoloy 800H & HT Technical Bulletin, in, Special Metals Corporation, 2004.

[39] Special Metals Inconel 600 Technical Bulletin, in, Special Metals Corporation, 2008.

[40] HASTELLOY® N Alloy Data Sheet, in, Haynes International, 2020.

[41] HAYNES® 282® Alloy Data Sheet, in, Haynes International, 2021.

[42] Specification Sheet: Alloy 316/316L (UNS S31600, S31603), in, Sandmeyer Steel Company, 2014.

[43] Specification Sheet: Alloy 347/347H (UNS S34700, S34709), in, Sandmeyer Steel Company, 2014.

[44] Specification Sheet: Alloy 304/304H (UNS S30400, S30409), in, Sandmeyer Steel Company, 2014.

[45] J.-w. Wang, C.-z. Zhang, Z.-h. Li, H.-x. Zhou, J.-x. He, J.-c. Yu, Corrosion behavior of nickel-based superalloys in thermal storage medium of molten eutectic NaCl-MgCl 2 in atmosphere, Solar Energy Materials and Solar Cells, 164 (2017) 146-155.

[46] W. Ding, A. Bonk, T. Bauer, Corrosion behavior of metallic alloys in molten chloride salts for thermal energy storage in concentrated solar power plants: A review, Frontiers of Chemical Science and Engineering, 12 (2018) 564-576.

[47] W. Yu, D. Singh, D.M. France, Investigation of Corrosion of 304 Stainless, Inconel 625, and Haynes 230 in a Chloride-Salt-Based Thermal Storage Medium, Journal of Materials Engineering and Performance, 28 (2019) 7379-7389.

[48] M. Alkhamis, Stability of Metal in Molten Chloride Salt at 800˚C, in: Chemical Engineering, The University of Arizona., 2016.

[49] H. Sun, P. Zhang, J. Wang, Effects of alloying elements on the corrosion behavior of Ni-based alloys in molten NaCl-KCl-MgCl2 salt at different temperatures, Corrosion Science, 143 (2018) 187-199.

[50] J.W. Ambrosek, Molten Chloride Salts for Heat Transfer in Nuclear Systems, in: Nuclear Engineering The University of Wisconsin - Madison, 2011.

[51] W. Ding, H. Shi, Y. Xiu, A. Bonk, A. Weisenburger, A. Jianu, T. Bauer, Hot corrosion behavior of commercial alloys in thermal energy storage material of molten MgCl2/KCl/NaCl under inert atmosphere, Solar Energy Materials and Solar Cells, 184 (2018) 22-30.

[52] B. Grégoire, C. Oskay, T.M. Meißner, M.C. Galetz, Corrosion mechanisms of ferritic-martensitic P91 steel and Inconel 600 nickel-based alloy in molten chlorides. Part I: NaCl–KCl binary system, Solar Energy Materials and Solar Cells, 215 (2020).

[53] F.B.H. H. Susskind, l. Green, S. Kalish, L.E. Kukacka,, A.E.W. W.E. McNulty, JR., Corrosion studies for a fused sait-liquid metal extraction process for the liquid metat fuel reactor, (1960).

[54] L. Guo, Q. Liu, H. Yin, T.J. Pan, Z. Tang, Excellent corrosion resistance of 316 stainless steel in purified NaCl-MgCl2 eutectic salt at high temperature, Corrosion Science, 166 (2020).

[55] G.Y. Lai, High-Temperature Corrosion and Materials Applications, ASM International, 2007.

[56] B. Liu, X. Wei, W. Wang, J. Lu, J. Ding, Corrosion behavior of Ni-based alloys in molten NaCl-CaCl 2 -MgCl 2 eutectic salt for concentrating solar power, Solar Energy Materials and Solar Cells, 170 (2017) 77-86.

[57] Z. Xu, B. Guan, X. Wei, J. Lu, J. Ding, W. Wang, High-temperature corrosion behavior of Inconel 625 alloy in a ternary molten salt of NaCl-CaCl2-MgCl2 in air and N2, Solar Energy, 238 (2022) 216-225.

[58] G. Salinas-Solano, J. Porcayo-Calderon, J.G. Gonzalez-Rodriguez, V.M. Salinas-Bravo, J.A. Ascencio-Gutierrez, L. Martinez-Gomez, High Temperature Corrosion of Inconel 600 in NaCl-KCl Molten Salts, Advances in Materials Science and Engineering, 2014 (2014) 1-8.

[59] S.S. Raiman, S. Lee, Aggregation and data analysis of corrosion studies in molten chloride and fluoride salts, Journal of Nuclear Materials, 511 (2018) 523-535.

[60] Standard Guide for Laboratory Immersion Corrosion Testing of Metals, in: Book of Standards, NACE International/ASTM International, 2021, pp. 10.